The Astronomical Journal, 171:359 (17pp), 2026 June https://doi.org/10.3847/1538-3881/ae5b6a

TOI-2494 c and TOI-5143 c: A Hot Saturn and a Hot Jupiter with Interior Planetary Companions

Samuel N. Quinn[1], Joseph E. Rodriguez[2], Karen A. Collins[1], Allyson Bieryla[1], W. J. Brennom[1], Jiayin Dong[3,4,54], Kyle Hixenbaugh[5], David W. Latham[1], Brandon T. Radzom[5], Andrew Vanderburg[1], Songhu Wang[5], Samuel W. Yee[1,53,55], George Zhou[6], Isabelle Boisse[7], Ilaria Carleo[8,9], Pia Cortés-Zuleta[10], Xavier Delfosse[11], Thierry Forveille[11], Davide Gandolfi[12], Elisa Goffo[12,13], Guillaume Hébrard[14,15], Neda Heidari[14], Flavien Kiefer[14], Eder Martioli[14,16], Grzegorz Nowak[8,9,17], Enric Palle[18], Rafael Brahm[19,20,21], Thomas Henning[22], Melissa J. Hobson[23], Matias Jones[24], Andrés Jordán[19,20,21], Chelsea X. Huang[6], Lizhou Sha[25], Alton Spencer[26], Ashley Ashiku[27], Khalid Barkaoui[28,29,30], Zouhair Benkhaldoun[31,32], Perry Berlind[1], Michael L. Calkins[1], Kevin I. Collins[33], Dennis M. Conti[34], Gilbert A. Esquerdo[1], Phil Evans[35], Mark E. Everett[36], Mourad Ghachoui[28,37], Michaël Gillon[28], Elisabeth Heldridge[27], Keith Horne[10], Steve B. Howell[38], Emmanuël Jehin[39], Christopher R. Mann[40], Adam Popowicz[41], Francisco J. Pozuelos[42], Justus J. Randolph[34], Howard M. Relles[1], Boris Safonov[43], Richard P. Schwarz[1], Jonathan J. Swift[27], Thiam-Guan Tan[44,45], Mathilde Timmermans[28], Cristilyn N. Watkins[1], Roberto Zambelli[46,47], Carl Ziegler[48], Jessie L. Christiansen[49], Tansu Daylan[50], Martin Paegert[1], Eric B. Ting[38], Jon M. Jenkins[38], George R. Ricker[51], Sara Seager[29], Roland K. Vanderspek[51], and Joshua N. Winn[52]

[1] Center for Astrophysics | Harvard & Smithsonian, 60 Garden Street, Cambridge, MA 02138, USA; squinn@cfa.harvard.edu
[2] Center for Data Intensive and Time Domain Astronomy, Department of Physics and Astronomy, Michigan State University, East Lansing, MI 48824, USA
[3] Center for Computational Astrophysics, Flatiron Institute, 162 Fifth Avenue, New York, NY 10010, USA
[4] Department of Astronomy, University of Illinois at Urbana-Champaign, Urbana, IL 61801, USA
[5] Department of Astronomy, Indiana University, Bloomington, IN 47405, USA
[6] Centre for Astrophysics, University of Southern Queensland, West Street, Toowoomba, QLD 4350, Australia
[7] Université Aix Marseille, CNRS, CNES, LAM, Marseille, France
[8] Instituto de Astrofísica de Canarias (IAC), E-38205 La Laguna, Tenerife, Spain
[9] Departamento de Astrofísica, Universidad de La Laguna (ULL), E-38206 La Laguna, Tenerife, Spain
[10] SUPA School of Physics & Astronomy, North Haugh, University of St Andrews, St Andrews KY16 9NS, UK
[11] Université Grenoble Alpes, CNRS, IPAG, 38000 Grenoble, France
[12] Dipartimento di Fisica, Universitá degli Studi di Torino, Via Pietro Giuria 1, I-10125 Torino, Italy
[13] Thüringer Landessternwarte Tautenburg, Sternwarte 5, D-07778 Tautenburg, Germany
[14] Institut d'Astrophysique de Paris, CNRS, UMR 7095, Sorbonne Université, 98 bis bd Arago, 75014 Paris, France
[15] Observatoire de Haute-Provence, CNRS, Université d'Aix-Marseille, 04870 Saint-Michel-l'Observatoire, France
[16] Laboratório Nacional de Astrofísica, Rua Estados Unidos 154, 37504-364, Itajubá, MG, Brazil
[17] Institute of Astronomy, Faculty of Physics, Astronomy and Informatics, Nicolaus Copernicus University, Torun, Poland
[18] Instituto de Astrofisica de Canarias, Via Lactea s/n, 38200 La Laguna, Tenerife, Spain
[19] Facultad de Ingeniera y Ciencias, Universidad Adolfo Ibáñez, Avenida Diagonal las Torres 2640, Peñalolén, Santiago, Chile
[20] Millennium Institute for Astrophysics, Chile
[21] Data Observatory Foundation, Chile
[22] Max-Planck-Institut für Astronomie, Königstuhl 17, Heidelberg 69117, Germany
[23] Observatoire de Genève, Département d'Astronomie, Université de Genève, Chemin Pegasi 51b, 1290 Versoix, Switzerland
[24] Instituto de Astronomía, Universidad Católica del Norte, Angamos 0610, 1270709, Antofagasta, Chile
[25] Department of Astronomy, University of Wisconsin-Madison, Madison, WI 53706, USA
[26] Western Connecticut State University, Danbury, CT 06810, USA
[27] The Thacher School, 5025 Thacher Road, Ojai, CA 93023, USA
[28] Astrobiology Research Unit, Université de Liège, Allée du 6 Août 19C, B-4000 Liège, Belgium
[29] Department of Earth, Atmospheric and Planetary Science, Massachusetts Institute of Technology, 77 Massachusetts Avenue, Cambridge, MA 02139, USA
[30] Instituto de Astrofísica de Canarias (IAC), Calle Vía Láctea s/n, 38200 La Laguna, Tenerife, Spain
[31] Department of Applied Physics and Astronomy, and Sharjah Academy for Astronomy, Space Sciences and Technology, University of Sharjah, UAE
[32] Cadi Ayyad University, Oukaimeden Observatory, High Energy Physics, Astrophysics and Geoscience Laboratory (LPAHGE), FSSM, Morocco
[33] George Mason University, 4400 University Drive, Fairfax, VA 22030, USA
[34] American Association of Variable Star Observers, 185 Alewife Brook Parkway, Suite 410, Cambridge, MA 02138, USA
[35] El Sauce Observatory, Coquimbo Province, Chile
[36] U.S. National Science Foundation National Optical-Infrared Astronomy Research Laboratory (NSF NOIRLab), Tucson, AZ, USA
[37] Oukaimeden Observatory, High Energy Physics and Astrophysics Laboratory, Cadi Ayyad University, Marrakech, Morocco
[38] NASA Ames Research Center, Moffett Field, CA 94035, USA
[39] Space Sciences, Technologies and Astrophysics Research (STAR) Institute, Université de Liège, Allée du 6 Août 19C, B-4000 Liège, Belgium
[40] National Research Council Canada, Herzberg Institute of Astrophysics, 5071 West Saanich Road, Victoria, BC V9E 2E7, Canada
[41] Faculty of Automatic Control, Electronics and Computer Science, Silesian University of Technology, Akademicka 16, 44-100 Gliwice, Poland
[42] Instituto de Astrofísica de Andalucía (IAA-CSIC), Glorieta de la Astronomía s/n, 18008 Granada, Spain
[43] Sternberg Astronomical Institute Lomonosov Moscow State University, Russia
[44] Perth Exoplanet Survey Telescope, Perth, WA, Australia
[45] Curtin Institute of Radio Astronomy, Curtin University, Bentley, WA 6102, Australia
[46] Società Astronomica Lunae, Castelnuovo Magra, Italy
[47] American Association of Variable Star Observers, 49 Bay State Road, Cambridge, MA 02138, USA
[48] Department of Physics, Engineering and Astronomy, Stephen F. Austin State University, 1936 North Street, Nacogdoches, TX 75962, USA
[49] NASA Exoplanet Science Institute, IPAC, Caltech, 1200 East California Avenue, Pasadena, CA 91125, USA
[50] Department of Physics and McDonnell Center for the Space Sciences, Washington University, St. Louis, MO 63130, USA
[51] Department of Physics and Kavli Institute for Astrophysics and Space Research, Massachusetts Institute of Technology, Cambridge, MA 02139, USA

[52] Department of Astrophysical Sciences, Princeton University, 4 Ivy Lane, Princeton, NJ 08544, USA
[53] Department of Physics & Astronomy, University of California, Los Angeles, Los Angeles, CA 90095, USA
Received 2025 September 26; revised 2026 March 17; accepted 2026 April 1; published 2026 May 19

Abstract

We present the TESS-based discoveries of planetary systems orbiting the late G dwarfs TOI-2494 and TOI-5143, each of which harbors a hot giant planet and a smaller interior planet. TOI-2494 hosts a transiting mini-Neptune ($P = 2.41$ days, $R_{\rm P} = 2.35^{+0.16}_{-0.15}\,R_\oplus$) and a hot Saturn ($P = 8.38$ days) with grazing transits, while TOI-5143 hosts a transiting mini-Neptune ($P = 2.38$ days, $R_{\rm P} = 2.73^{+0.19}_{-0.17}\,R_\oplus$) and a hot Jupiter ($P = 5.21$ days) with grazing transits. We measure the masses of TOI-2494 c ($80 \pm 19\,M_\oplus$) and TOI-5143 c ($208 \pm 14\,M_\oplus$), place upper limits on the masses of the smaller planets, and explore the architectures of the planetary systems. TOI-2494 c and TOI-5143 c join a small but growing number of short-period giant planets known to be flanked by smaller companions. While the absence of close neighbors to most hot Jupiters would be consistent with disruptive dynamical evolution, the presence of nearby small planets in some hot Jupiter systems points to a separate, dynamically quiet formation pathway. In support of this conclusion, we present preliminary evidence that hot giant planets with small nearby companions tend to have low mutual orbital inclinations, consistent with the mutual inclination distribution of the dynamically quiet population of compact systems of multiple super-Earths and mini-Neptunes.

Unified Astronomy Thesaurus concepts: Hot Jupiters (753); Exoplanet evolution (491); Exoplanet migration (2205); Exoplanets (498); Mini-Neptunes (1063); Exoplanet systems (484)

Materials only available in the online version of record: machine-readable table

1. Introduction

Giant planets are believed to form primarily by core-nucleated runaway gas accretion beyond the snow line, where the surface density of silicates and ices in the protoplanetary disk is high (see, e.g., J. J. Lissauer 1993). Fittingly, beyond the snow line is where Jovian planets are most common, with about 14% of Sun-like stars hosting a giant planet orbiting between 2 and 8 au (B. J. Fulton et al. 2021). Nevertheless, Jovian planets are sometimes observed at very small separations ($a \lesssim 0.1$ au). While they are much less common than their long-period counterparts (between about 0.4% and 1.2%; E. L. Wright et al. 2010; F. Fressin et al. 2013; G. Zhou et al. 2019), hot Jupiters are overrepresented in transit and Doppler surveys because they are biased toward finding and characterizing large and short-period companions. Even though hot Jupiters are not typical of the giant planet formation process, they are valuable in that they constitute the largest population of transiting giant planets to study. By virtue of their short periods, frequent transits, and high equilibrium temperatures, they also provide observational access to the physical processes that shape the population—access that is much harder to achieve for planets with wider orbits.

Whether and how the hot Jupiters migrated from their birthplaces beyond the snow line is an open question. Massive planets can move inward through angular momentum exchange with the gas disk (P. Goldreich & S. Tremaine 1980; D. N. C. Lin et al. 1996), or through excitement of extreme eccentricity followed by tidal friction with the host star to shrink the orbit. These high-eccentricity migration (HEM) mechanisms may include planet–planet scattering (e.g., F. C. Adams & G. Laughlin 2003; S. Chatterjee et al. 2008), interaction with a massive, distant companion via the Kozai–Lidov effect (Y. Kozai 1962; M. L. Lidov 1962; D. Fabrycky & S. Tremaine 2007), or secular interactions between planets (S. Naoz et al. 2011; Y. Wu & Y. Lithwick 2011). It may even be possible for some hot Jupiters to form in situ (K. Batygin et al. 2016; A. C. Boley et al. 2016). Because no single proposed mechanism seems capable of producing the observed population, it seems likely that realistic models of hot Jupiter formation will have to incorporate multiple formation pathways to explain all the observations. New discoveries and further analysis of known planets can help constrain these models.

There are many possible observational approaches to constrain migration pathways, each with its merits. Because disk-driven migration is likely to preserve low eccentricities while HEM should initially excite high eccentricities before being modified over time by tidal interactions, the importance of these mechanisms can be constrained by the observed distribution of hot Jupiter eccentricities (e.g., S. N. Quinn et al. 2014; J. E. Rodriguez et al. 2023; S. W. Yee et al. 2023; J. Schulte et al. 2024), or by the observed frequency of highly eccentric migrating Jupiters (A. Socrates et al. 2012; R. I. Dawson et al. 2015). Similarly, disk-driven migration should generally leave the planet on an orbit that is well aligned with the stellar spin, while some three-body interactions can be expected to produce misaligned orbits. The distribution of stellar obliquities can therefore be considered a tracer of dynamical history (e.g., K. C. Schlaufman 2010; J. N. Winn et al. 2010), though this is complicated by physical processes that might modify spin–orbit alignment during or after migration (e.g., tides). An alternative explanation for spin–orbit misalignment is that the primordial disk is misaligned by an external perturber (K. Batygin 2012; M. Xiang-Gruess 2016), which could lead to inclined orbits even for disk migration. It has also been proposed that a massive star can misalign itself from the disk via the effect of internal gravity waves (T. M. Rogers et al. 2012). Recent work from M. Rice et al. (2022) and X.-Y. Wang et al. (2024), though, shows that known warm Jupiters orbiting single stars tend to be well aligned, which would not be the case if the host stars themselves cause the misalignment. At least among

[54] Flatiron Research Fellow.
[55] 51 Pegasi b Fellow.

Table 1
Literature and Measured Properties for TOI-2494 and TOI-5143

Parameter	Description	TOI-2494	TOI-5143	References
α_{J2000}[a]	R.A.	06:00:38.271	11:01:27.680	(1)
δ_{J2000}[a]	Decl.	+00:07:54.373	+05:08:22.131	(1)
G	Gaia G mag	11.23 ± 0.02	11.81 ± 0.02	(1)
BP	Gaia BP mag	11.66 ± 0.02	12.26 ± 0.02	(1)
RP	Gaia RP mag	10.68 ± 0.02	11.21 ± 0.02	(1)
T	TESS mag	10.720 ± 0.0062	11.267 ± 0.0066	(2)
TIC	TESS Input Catalog (TIC) ID	282576340	281837575	(3)
J	Two Micron All Sky Survey (2MASS) J mag	10.042 ± 0.024	10.474 ± 0.026	(4)
H	2MASS H mag	9.660 ± 0.022	10.101 ± 0.024	(4)
K_S	2MASS K_S mag	9.602 ± 0.020	9.980 ± 0.020	(4)
WISE1	Wide-field Infrared Survey Explorer (WISE) WISE1 mag	9.537 ± 0.030	9.920 ± 0.030	(5)
WISE2	WISE2 mag	9.602 ± 0.030	9.965 ± 0.030	(5)
WISE3	WISE3 mag	9.585 ± 0.045	9.799 ± 0.058	(5)
μ_α	Gaia Data Release 2 (DR2) R.A. proper motion (mas yr^{-1})	15.727 ± 0.017	−49.326 ± 0.017	(1)
μ_δ	Gaia DR2 decl. proper motion (mas yr^{-1})	−66.981 ± 0.015	0.114 ± 0.016	(1)
π[b]	Gaia DR2 parallax (mas)	6.543 ± 0.045	5.515 ± 0.072	(1)

Notes. Photometric uncertainties include a systematic error floor.
[a] R.A. and decl. are in epoch J2000. The coordinates come from Vizier where the Gaia R.A. and decl. have been precessed and corrected to J2000 from epoch J2015.5.
[b] Values have been corrected for the –0.30 μas offset as reported by L. Lindegren et al. (2018) but this is not significant for these systems.
References. (1) Gaia Collaboration et al. (2018), (2) E. Høg et al. (2000), (3) K. G. Stassun et al. (2019), (4) R. M. Cutri et al. (2003), and (5) R. M. Cutri et al. (2012).

currently detected warm Jupiter hosts, primordial disk misalignment does not appear to be prevalent.

The architecture of a planetary system can also provide clues about how it formed. The occurrence rate of distant stellar and planetary companions to hot Jupiters, for example, could reveal whether these star–planet and planet–planet interactions could be primarily responsible for hot Jupiter migration. Some distant companions have been discovered, but there is not solid evidence that these companions are frequent enough and have the necessary properties to explain the majority of hot Jupiters (e.g., H. A. Knutson et al. 2014; H. Ngo et al. 2016). On the other hand, the existence of planets on nearby, inner orbits ($a_{\rm out} \lesssim 2a_{\rm in}$) can rule out migration that requires high eccentricities; such systems would not have survived the high-eccentricity phase of the migrating giant planet when its close approach to the star was a factor of 2 smaller than its final semimajor axis (A. J. Mustill et al. 2015). A small number of hot Jupiters has indeed been found to have interior, small planetary companions (J. C. Becker et al. 2015; C. I. Cañas et al. 2019; C. X. Huang et al. 2020a; B. J. Hord et al. 2022; G. Maciejewski et al. 2023; L. Sha et al. 2023; J. Korth et al. 2024). While HEM is not a viable explanation for these planets, it is not yet clear how common these are.

In this paper, we present the discovery and characterization of two planetary systems, each of which features a close-orbiting giant planet and an interior mini-Neptune that could not have survived HEM migration. In Section 2, we describe the transit photometry, radial velocities (RVs), and high-resolution imaging that we use to characterize the systems, and in Section 3, we present the global modeling of the data and derived stellar and planetary parameters. Finally, in Section 4, we discuss these and similar systems in the context of hot Jupiter formation and consider additional observations that can shed light upon the formation process before summarizing the discoveries in Section 5.

2. Observations

2.1. TESS Photometry

NASA's TESS mission (G. R. Ricker et al. 2015) has been surveying the sky since 2018. It uses four cameras arranged in a 24° × 96° configuration and observes an approximately antisolar field for 27.4 days at a time before changing fields. The data for a subset of preselected stars are available with a 20 s or a 2 minute cadence, and the full imaging data are available at a more modest cadence. During its 2 yr prime mission, these full frame images (FFIs) were obtained with a 30 minute cadence. Later the FFI cadence was improved to 10 minutes, and most recently it was improved still further to 200 s. The 2 minute cadence data are processed by the Science Processing Operations Center (SPOC) at NASA Ames (J. M. Jenkins et al. 2015, 2016), with procedures adapted from the pipeline originally developed for the Kepler mission (J. M. Jenkins et al. 2010). SPOC produces two versions of the extracted 2 minute light curves: simple aperture photometry (SAP), and the presearch data conditioning (PDC) version used in the transiting planet search (see M. C. Stumpe et al. 2012). PDC light curves have been corrected for systematics on several timescales using the cotrending basis vectors (CBVs), and are usually the better choice for transiting planet detection and characterization. For some targets, SPOC also produces FFI light curves with data products similar to those from the 2 minute data (D. A. Caldwell et al. 2020). All of the TESS data used in this paper are described in the following sections and can be found in MAST at DOI:10.17909/arz7-bt05 (S. Quinn 2025).

2.1.1. TOI-2494

TIC 282576340 is a G dwarf at a distance of about 150 pc, which makes it bright enough ($T = 10.7$, $V = 11.5$, and $K = 9.6$) to obtain good photometric precision with TESS

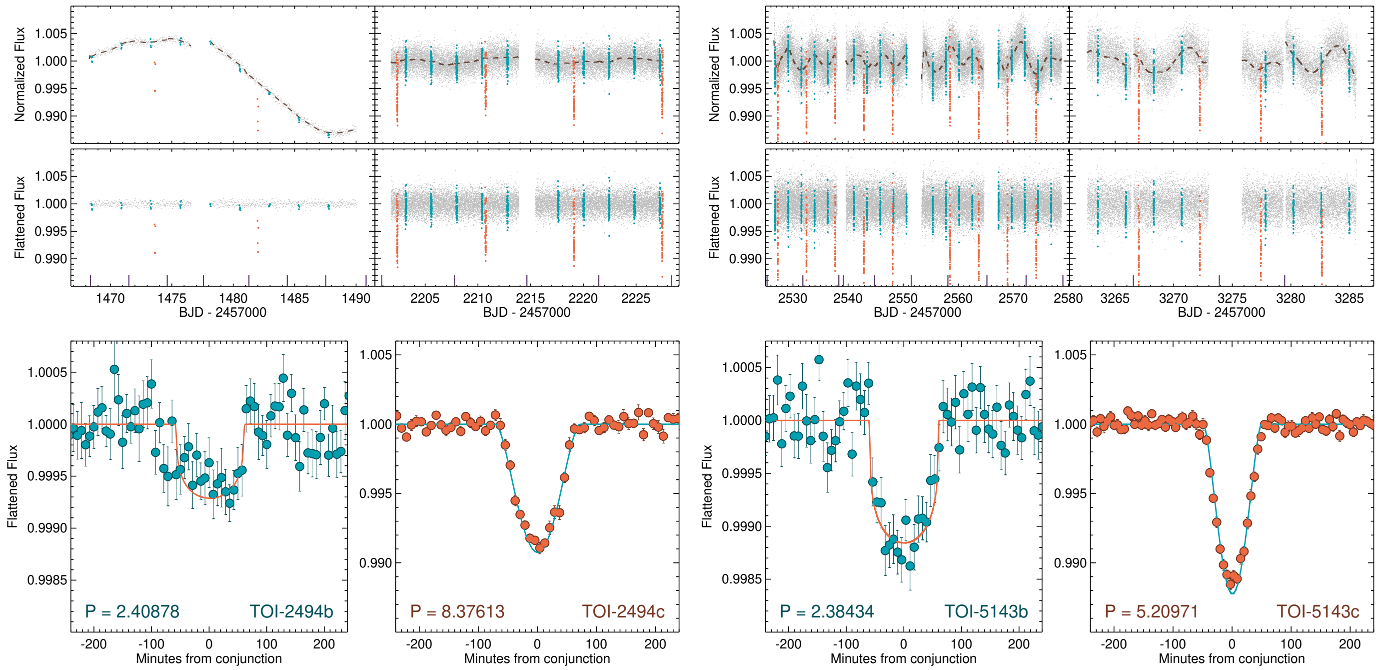

Figure 1. Top panels: the normalized raw and flattened TESS light curves of TOI-2494 (left) and TOI-5143 (right). Individual cadences are plotted as small gray points. Note that Sector 6 data for TOI-2494 were extracted from the 30 minute FFIs, while all other datasets shown are the SPOC PDCSAP 2 minute cadence data. In-transit data for planets b and c in each system are colored blue and orange, respectively. The out-of-transit spline models used to flatten the light curves are shown as a dashed brown line. The times of reaction wheel desaturation events, which often induce discontinuities in the light curve and are used as additional spline break points, are marked in purple along the *x*-axes. Bottom panels: the binned, phase-folded TESS light curves of TOI-2494 b and c (left) and TOI-5143 b and c (right), along with the best-fit `EXOFASTv2` transit models. Note that the shallow transits and the deeper transits are plotted with different *y*-axis scales for improved visibility of transit shapes.

and high-signal-to-noise-ratio follow-up observations. See Table 1 for its basic photometric and astrometric properties. It was observed in the FFIs in Sector 6 with a cadence of 30 minutes between 2018 December 11 and 2019 January 7, and then reobserved in Sector 33 during the first extended mission with a cadence of 2 minutes between 2020 December 18 and 2021 January 13. The TESS mission designated the star as TESS Object of Interest (TOI) TOI-2494 in 2021 February when a planet candidate was identified using FFI light curves extracted with the Quick Look Pipeline (C. X. Huang et al. 2020b, 2020c). The candidate, TOI-2494.01, had a transit depth and orbital period consistent with a hot Jupiter. A second candidate, TOI-2494.02, with a smaller transit depth and shorter orbital period, was identified 2 months later. We leave details of the candidates to Section 3, where we describe our fitting methodology and results.

In the global fit of the TOI-2494 system described in Section 3, we used the SPOC PDC 2 minute light curve from Sector 33. In Sector 6, however, there was no SPOC-FFI light curve produced for TOI-2494, so we extracted our own 30 minute light curve from the Sector 6 FFIs based on the process outlined in A. Vanderburg et al. (2019). This process is described in detail for FFI data in J. E. Rodriguez et al. (2023), but we also summarize it here for convenience. We began by extracting the light curve in a series of apertures of varying size and decorrelated each against the means and standard deviations of the spacecraft quaternion time series within each photometric exposure, as well as the SPOC CBVs (binned to 30 minutes). We also included a simultaneous basis spline fit to account for the stellar variability, and iteratively performed outlier rejection in the linear regression. We subtracted the best-fit systematics correction and then corrected for dilution in each aperture based on the modeled TESS pixel response function and the known nearby stars. We selected the aperture that minimizes the scatter in the out-of-transit flux as our final light curve.

Before fitting, we flattened the light curves using the basis spline routine `Keplerspline`[56] (A. Vanderburg & J. A. Johnson 2014). To optimize the spacing for the break points (to properly account for discontinuities in the data), we followed the methodology from C. J. Shallue & A. Vanderburg (2018). The extracted, flattened, and folded light curves are shown in Figure 1.

2.1.2. TOI-5143

TIC 281837575 is a G dwarf at a distance of 180 pc, making it slightly fainter than TOI-2494, but still bright enough for precise photometry and follow-up observations ($T = 11.3$, $V = 11.9$, and $K = 10.0$). Its photometric and astrometric properties are also listed in Table 1. TIC 281837575 lies in the narrow band near the ecliptic plane that was not observed during the TESS prime mission, but it was observed during the first extended mission in Sectors 45 and 46 at 2 minute cadence. These observations spanned approximately 55 days from 2021 November 6 to December 30. The TESS mission designated the star TOI-5143 in 2022 January. Two candidates were reported, including one consistent with a hot Jupiter and a second with a shallower transit and a shorter period.[57] We adopted the SPOC PDC 2 minute light curve from Sectors 45 and 46 for our global fit of the TOI-5143 system. Similar to

[56] https://github.com/avanderburg/keplerspline

[57] This system was independently reported as a community TOI on ExoFOP earlier that month by A. Spencer. See https://exofop.ipac.caltech.edu/tess/view_tag.php?tag=104042.

TOI-2494, we flattened the light curve using Keplerspline (A. Vanderburg & J. A. Johnson 2014). The extracted, flattened, and folded light curves are shown in Figure 1.

2.2. Ground-based Photometry

Because the TESS pixel scale is ∼21″ pixel^{-1}, even when a photometric aperture is as small as a few pixels across (∼1′), the aperture often includes significant light from multiple stars. To determine the true source of the TOI-2494 and TOI-5143 signals in the TESS data, improve the transit ephemerides, monitor for transit timing variations (TTVs), and independently check the TESS transit depths, we conducted ground-based light-curve follow-up observations of the fields around TOI-2494 and TOI-5143 as part of the TESS Follow-up Observing Program[58] (TFOP; K. Collins 2019) Sub Group 1 (SG1). We used the TESS Transit Finder, which is a customized version of the Tapir software package (E. Jensen 2013), to schedule our transit observations. The light-curve follow-up observations are summarized in Table 2 and described below. All reduced data products are available on the ExoFOP website (NExScI 2022).[59]

Most of the ground-based photometric observations were extracted using the AstroImageJ (AIJ) software package (K. A. Collins et al. 2017), including those from the LCOGT (T. M. Brown et al. 2013), a network of 2.0 m, 1.0 m and 0.4 m telescope nodes that are distributed in latitude and longitude, and which are equipped with a MuSCAT3 multiband imager (N. Narita et al. 2020), Sinistro cameras, and SBIG STX6303 cameras, respectively. Prior to extraction, the images were calibrated by the standard LCOGT BANZAI pipeline (C. McCully et al. 2018). Other datasets extracted with AIJ include those from Whipple Observatory in Arizona, El Sauce Observatory in Chile, Thacher Observatory in California, the TRAPPIST North telescope in Morocco, the SUTO telescope in Spain, and the North Oconee Observatory in Georgia.

Data from the Dragonfly Telephoto Array in New Mexico were reduced and analyzed with a custom differential aperture photometry pipeline, and those from PEST in Australia relied on a custom pipeline based on C-Munipack.[60] Data from the MuSCAT2 multicolor imager (N. Narita et al. 2019) on the 1.52 m Telescopio Carlos Sanchez at Teide Observatory, Spain were analyzed with the dedicated MuSCAT2 photometry pipeline, as described in H. Parviainen et al. (2019).

Some additional details of these observations are given in Table 2, and the data are shown in Figure 2.

2.3. High-resolution Imaging

While Gaia can detect most stars separated by more than 1″ from the brightest star in the aperture, high-resolution imaging is needed to confidently exclude the presence of faint stars within 1″, which could in principle be the true sources of the transit events that we have detected.

2.3.1. TOI-2494 Imaging

We observed TOI-2494 on UT 2021 February 27 in the *I* band (879 nm) with the HRCam speckle imager (A. Tokovinin 2018) on the 4.1 m Southern Astrophysical Research (SOAR) telescope on Cerro Pachón in Chile. The data had a point-spread function (PSF) of 0.″064 and reached a contrast of 6.8 mag at a separation of 1″. No nearby stellar companions were detected. The contrast curve is shown in Figure 3.

2.3.2. TOI-5143 Imaging

We observed TOI-5143 with the speckle polarimeter on the 2.5 m telescope at the Caucasian Mountain Observatory of Sternberg Astronomical Institute (SAI) of Lomonosov Moscow State University (B. S. Safonov et al. 2017) on UT 2022 March 21, and again on UT 2022 December 2. Observations

Table 2
Ground-based Transit Observations

Planet	Date (UT)	Telescope	Filter(s)	Span
TOI-2494 b[a]	2021-10-02	LCO-CTIO 1.0 m	*ip*	Full
TOI-2494 b[a]	2022-01-13	MuSCAT2 1.52 m	*gp*, *rp*, *ip*, *zs*	Full
TOI-2494 c[a]	2021-03-04	FLWO 1.2 m	*ip*	Ingr.
TOI-2494 c[a]	2021-03-21	El Sauce 0.51 m	*Rc*	Egr.
TOI-2494 c[a]	2021-10-15	CHAT 0.7 m	*rp*	Ingr.
TOI-2494 c[a]	2021-11-26	CHAT 0.7 m	*rp*	Full
TOI-2494 c[a]	2022-03-16	Dragonfly 1.0 m	*gp*, *rp*	Full
TOI-2494 c[a]	2022-12-17	LCO-SSO 1.0 m	*gp*, *zs*	Full
TOI-5143 b	2022-03-12	FLWO 1.2 m	*ip*	Full
TOI-5143 b	2022-03-31	FLWO 1.2 m	*ip*	Full
TOI-5143 b	2022-04-04	LCO-CTIO 1.0 m	*ip*	Full
TOI-5143 b	2022-04-19	MuSCAT3 2.0 m	*gp*, *rp*, *ip*, *zs*	Full
TOI-5143 b	2022-04-23	LCO-CTIO 1.0 m	*ip*	Full
TOI-5143 b	2022-05-03	LCO-SAAO 1.0 m	*ip*	Full
TOI-5143 b	2022-06-03	LCO-SAAO 1.0 m	*ip*	Full
TOI-5143 b	2022-12-11	MuSCAT3 2.0 m	*gp*, *rp*, *ip*, *zs*	Full
TOI-5143 b	2022-12-21	LCO-Teid 1.0 m	*ip*	Full
TOI-5143 b	2022-12-28	LCO-CTIO 1.0 m	*ip*	Full
TOI-5143 b	2023-01-09	LCO-Teid 1.0 m	*ip*	Full
TOI-5143 b	2023-02-02	LCO-SAAO 1.0 m	*ip*	Full
TOI-5143 b	2023-02-13	LCO-Teid 1.0 m	*ip*	Full
TOI-5143 b	2023-02-16	LCO-McD 1.0 m	*ip*	Full
TOI-5143 b	2023-02-21	LCO-CTIO 1.0 m	*ip*	Full
TOI-5143 c[a]	2022-01-30	MuSCAT2 1.52 m	*gp*, *rp*, *ip*, *zs*	Full
TOI-5143 c[a]	2022-02-05	FLWO 1.2 m	*ip*	Full
TOI-5143 c[a]	2022-02-15	PEST 0.3 m	*rp*	Full
TOI-5143 c	2022-03-02	Oconee 0.11 m	clear	Full
TOI-5143 c	2022-03-18	SUTO1 0.3 m	*B*	Full
TOI-5143 c	2022-03-24	FLWO 1.2 m	*ip*	Full
TOI-5143 c[a]	2022-04-19	FLWO 1.2 m	*B*, ip	Full
TOI-5143 c[a]	2022-05-04	LCO-SAAO 1.0 m	*ip*	Full
TOI-5143 c[a]	2022-12-19	TRAPPIST-N 0.6 m	*zp*	Full
TOI-5143 c[a]	2022-12-25	LCO-CTIO 1.0 m	*ip*	Full
TOI-5143 c	2022-12-25	LCO-CTIO 0.4 m	*ip*	Full
TOI-5143 c	2023-01-20	Thacher 0.7 m	*rp*	Full
TOI-5143 c	2023-02-04	LCO-Teid 1.0 m	*ip*	Ingr.
TOI-5143 c[a]	2023-02-04	LCO-SSAO 1.0 m	*ip*	Full
TOI-5143 c[a]	2023-02-20	LCO-SSO 1.0 m	*ip*	Full
TOI-5143 c	2023-02-20	LCO-SSO 0.4 m	*ip*	Ingr.

Note.
[a] Indicates observations that were used in the global fit. The filter bands designated as *gp*, *rp*, *ip*, and *zs* are the Sloan g', Sloan r', Sloan i', and Pan-STARRS *z*-short bands, respectively. The Las Cumbres Observatory Global Telescope (LCOGT) telescope nodes designated a s Cerro Tololo Inter-American Observatory (CTIO), SAAO, Teide, McD, and SSO are located at CTIO, South Africa Astronomical Observatory, Teide Observatory, McDonald Observatory, and Siding Spring Observatory, respectively.

[58] https://tess.mit.edu/followup
[59] https://exofop.ipac.caltech.edu/tess/
[60] http://c-munipack.sourceforge.net

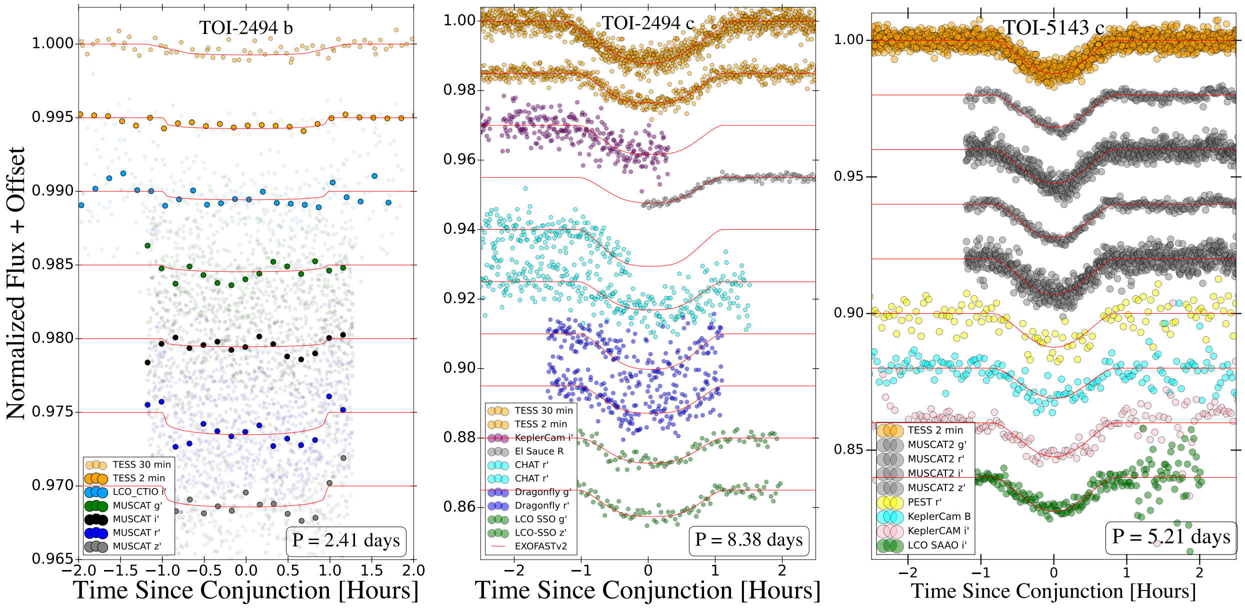

Figure 2. The TESS 30 minute cadence (orange), 2 minute cadence (blue), and TFOP SG1 follow-up transits of TOI-2494 b (left), TOI-2494 c (middle), and TOI-5143 c (right). The EXOFASTv2 model for each transit observation is shown by the red solid line.

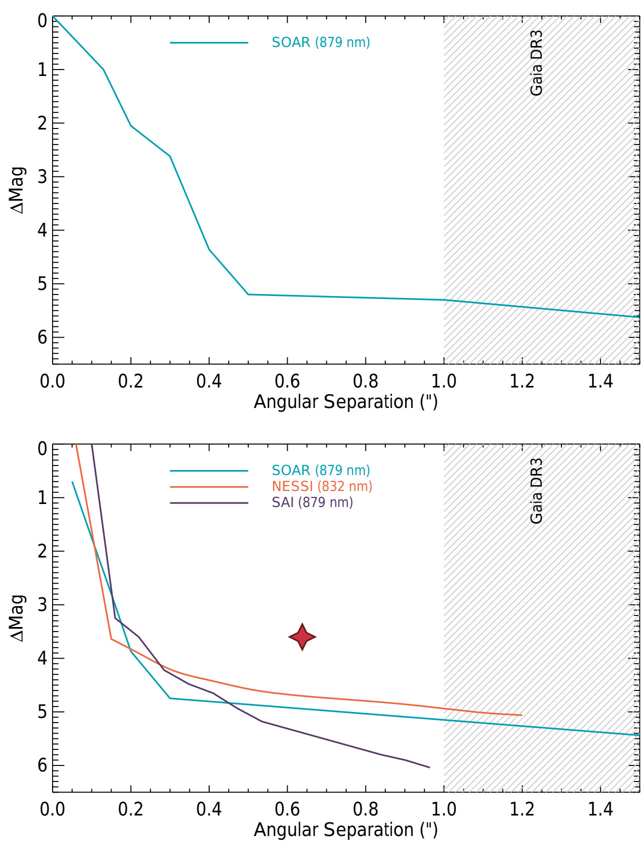

Figure 3. The high-resolution imaging contrast curves for TOI-2494 (top) and TOI-5143 (bottom). Each instrument is plotted in a different color, and the gray shaded region illustrates approximately where Gaia Data Release 3 (DR3) would be sensitive to most companions. For TOI-5143, all observations detect a nearby companion, which is shown as a red star.

were taken in I band (879 nm), achieved a PSF width of 0$''\!.$083, and reached contrasts of 6.1 and 5.9 mag, respectively, at a separation of 1$''$. Similar I-band speckle observations were obtained on UT 2022 April 15 with HRCam on the 4.1 m SOAR telescope. These data had a PSF width of 0$''\!.$064 and reached a contrast of 6.4 mag at 1$''$. Finally, we used the NN-EXPLORE Exoplanet Stellar Speckle Imager (NESSI; N. J. Scott et al. 2018) on the WIYN 3.5 m telescope at Kitt Peak Observatory on UT 2022 April 18 to observe TOI-5143 in a narrow filter centered on 832 nm. The NESSI PSF was 0$''\!.$02 and achieved a contrast of 4.9 mag at 1$''$.

All three facilities detected a nearby star (see Figure 3), for which we measured a separation of 0$''\!.$638 $\pm$ 0$''\!.$003 at a position angle of 295$^\circ\!.$0 $\pm$ 0$^\circ\!.$1 relative to TOI-5143. The I-band magnitude difference is $\Delta I = 3.6 \pm 0.3$. Given the distance to the system (182 pc), the projected separation is 116 au, and the magnitude difference suggests an early to mid M dwarf if it is physically associated with TOI-5143. The presence of such a stellar companion would not be surprising; previous studies have shown that while close binaries ($\lesssim$50 au) can influence the formation or survival of planetary systems, planet occurrence rates in wide binaries and around single stars are similar (e.g., A. L. Kraus et al. 2016; R. A. Matson et al. 2018; K. V. Lester et al. 2021). Below, we use statistical arguments and our high-resolution imaging data to demonstrate that the nearby companion is indeed a physically bound M dwarf and hereafter refer to it as TOI-5143 B.

Based on the number density of nearby stars in Gaia DR3, we expect to detect 2.6×10^{-4} background stars in our speckle images within 1$''$, and only 2.4×10^{-5} stars as close and bright as TOI-5143 B. Contrariwise, we do expect to detect physically bound companions quite frequently at the distance of TOI-5143, given the projected separations to which the speckle imaging is sensitive (18–180 au). Sun-like stars host binary companions at a rate of ∼46%, and the peak of the separation distribution is near 50 au (D. Raghavan et al. 2010); approximately 12% of all Sun-like stars host a binary companion with a semimajor axis between 18 and 180 au. Most of these bound companions would be bright enough to be detected in our speckle imaging. This suggests that it is roughly 1000 times more likely that TOI-5143 B is a bound companion than a background star. Moreover, relative astrometry from the two epochs of SAI imaging reveals no

Table 3
Radial Velocities of TOI-2494 and TOI-5143

Star	BJD_{TDB} (days)	Instrument	RV (m/s^{-1})	σ_{RV} (m/s^{-1})
TOI-2494	2459313.492400	CHIRON	−24,101.7	20.0
TOI-2494	2459484.893390	FEROS	−24,055.8	6.5
TOI-2494	2459271.776537	TRES	−24,138.1	18.7
TOI-5143	2459664.539475	HARPS-N	13,223.2	2.1
TOI-5143	2459645.833982	NEID	13,391.5	4.3
TOI-5143	2459687.414870	SOPHIE	13,361.9	8.0
TOI-5143	2459663.788829	TRES	13,233.6	19.0

Note. The full table is provided in machine-readable format. A portion is shown here to demonstrate its form and content. The velocities from each instrument have been shifted to an absolute velocity zero-point scale, determined from Tillinghast Reflector Echelle Spectrograph (TRES) observations of minor planets and the fitted instrument offsets from EXOFASTv2. The uncertainties have not been inflated to reflect the uncertainty in these shifts, nor do they include the derived instrumental jitter terms reported in Table 5. If the reader wishes to fit the data, instrument offsets and jitter terms should still be included as free parameters.

(This table is available in its entirety in machine-readable form in the online article.)

significant relative motion (2.9 ± 8.1 mas); in the 0.7 yr between observations, the measured proper motion of TOI-5143 would have displaced it by 34.5 mas relative to a distant background star.

2.4. Spectroscopy

Below we describe our spectroscopic observations of TOI-2494 and TOI-5143, the facilities we used, and the analyses used to extract RVs and estimate the spectroscopic parameters of the host stars. The RVs are reported in Table 3 and shown in Figure 4.

As we subsequently describe in Section 3, we used the spectroscopically derived metallicities as priors in the global fits because they are difficult to derive precisely using other means. We did not enforce priors on the spectroscopic temperatures and surface gravities due to the degeneracies between these parameters in the emergent stellar spectrum. However, we do report these spectroscopically derived values in the text below for both stars, and we note that the final stellar parameters from the global fits are consistent with the spectroscopic estimates, validating the accuracy of the spectroscopic T_{eff}, $\log g$, and importantly, the [Fe/H] for these stars.

2.4.1. TOI-2494 Radial Velocities

We observed TOI-2494 with the CHIRON high-resolution echelle spectrograph mounted on the 1.5 m SMARTS telescope at CTIO in Chile (A. Tokovinin et al. 2013). The 26 observations spanned 7 months from 2021 April 8 and 2021 November 11, with typical exposure times of 33 minutes. The data were taken in CHIRON's slicer mode, which uses a fiber-fed image slicer to achieve a resolving power of $R \sim 80{,}000$ covering a wavelength range between 4100 and 8700 Å. We used the optimal extraction provided by the CHIRON team, as described in L. A. Paredes et al. (2021), and derived RVs by fitting the spectral line profiles, measured via least-squares deconvolution of the observed spectra against synthetic templates (J.-F. Donati et al. 1997; G. Zhou et al. 2018). We found no evidence for composite line profiles or line profile shape variations, and conclude that the observed velocity variation is due to one or more companions orbiting TOI-2494.

We also observed TOI-2494 with TRES (G. Fűrész 2008) on the 1.5 m Tillinghast Reflector at the Fred L. Whipple Observatory (FLWO) on Mount Hopkins in Arizona, USA. TRES is a fiber-fed echelle spectrograph with a resolving power of $R \sim 44{,}000$ and wavelength coverage from 3850 to 9100 Å. Five TRES spectra were obtained between 2021 February 21 and 2021 April 13, achieving a typical signal-to-noise ratio of 30 per resolution element. We reduced the spectra and extracted RVs following procedures outlined in L. A. Buchhave et al. (2010), and corrected for instrumental drift using standard stars following S. N. Quinn et al. (2014).

Lastly, five spectra were obtained using FEROS (A. Kaufer et al. 1999) on the 2.2 m MPG/ESO telescope at La Silla, Chile. FEROS has a resolving power of $R \sim 48{,}000$ and a wavelength coverage spanning 3500–9200 Å. FEROS spectra were obtained between 2021 September 27 and 2021 November 21, and were reduced, extracted, and analyzed using ceres (R. Brahm et al. 2017).

2.4.2. TOI-2494 Spectroscopic Stellar Parameters

We estimated the effective temperature (T_{eff}), surface gravity ($\log g$), and metallicity ([Fe/H]) of TOI-2494 from the CHIRON spectrum by matching against a library of observed spectra that have been previously classified by stellar parameter classification (SPC; L. A. Buchhave et al. 2012). Interpolation of the library was performed via a gradient-boosting regressor implemented in the scikit-learn Python module. We found $T_{eff} = 5492 \pm 50$ K, $\log g = 4.49 \pm 0.10$, and $[Fe/H] = +0.03 \pm 0.08$, where the uncertainties are floor errors assigned based on the known performance of SPC, because the internal errors derived from the scatter in the CHIRON classifications are smaller than is believable. We provided the metallicity as a prior to the global fit described in Section 3. We measured the projected rotational velocity to be $v \sin i_\star = 2.5 \pm 1.0$ km s^{-1}, but the instrumental resolving power is only 3.7 km s^{-1}. For such slow rotation, we caution that this estimate may suffer systematic offsets. This value is broadly consistent with the appearance of periodic variation in the TESS light curve with a timescale of roughly 20 days; if caused by rotating surface features, the photometric modulation would imply an equatorial rotational velocity of about 2.3 km s^{-1}. While these values suggest the stellar spin and orbital axes may be well aligned, more reliable measurements would be needed to draw quantitative conclusions.

We also derived spectroscopic stellar parameters by running SPC on the TRES spectra and obtained results consistent with our analysis of CHIRON spectra: $T_{eff} = 5475 \pm 50$ K, $\log g = 4.59 \pm 0.10$, and $[Fe/H] = +0.15 \pm 0.08$. The rotational broadening was estimated to be 2.9 ± 1.0 km s^{-1}, similar to the value derived from the CHIRON spectra. We note that the TRES instrumental line profiles are broader than those from CHIRON, so this number is somewhat more susceptible to systematics. The broadening reported by SPC may also include a small contribution from the macroturbulent velocity, which is only treated in the synthetic templates using a fixed value of $v_{mac} = 1$ km s^{-1}.

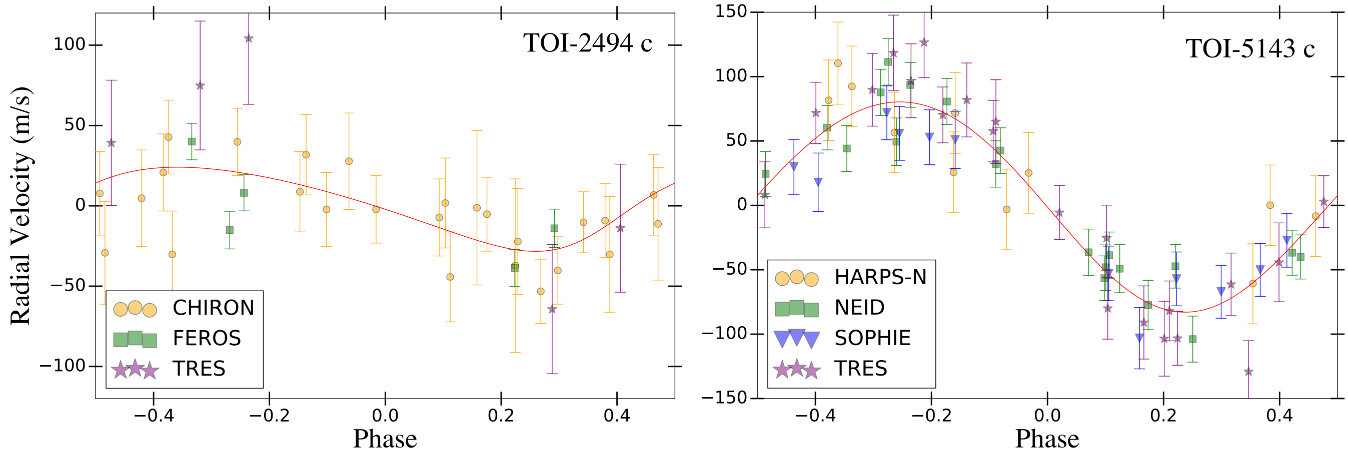

Figure 4. Left: RV measurements from CHIRON (orange), Fiber-fed Extended Range Optical Spectrograph (FEROS; green), and TRES (purple) for TOI-2494. The RVs are phase folded to the best-fit period for TOI-2494 c, as determined by the EXOFASTv2 global fit. Right: RV measurements from HARPS-N (orange), NEID (green), SOPHIE (blue), and TRES (purple) for TOI-5143, phase folded to the best-fit period of TOI-5143 c, as determined by EXOFASTv2. The best-fit model in each panel is shown in red.

2.4.3. TOI-5143 Radial Velocities

We obtained high-resolution spectra of TOI-5143 with four different facilities: TRES on the 1.5 m at FLWO in Arizona; NEID (S. Halverson et al. 2016; C. Schwab et al. 2016) on the 3.5 m WIYN telescope at the Kitt Peak National Observatory in Arizona; SOPHIE (S. Perruchot et al. 2008; F. Bouchy et al. 2009) on the 1.93 m at the Observatoire de Haute-Provence, France; and HARPS-N (R. Cosentino et al. 2012, 2014) on the 3.58 m Italian Telescopio Nazionale Galileo at the Roque de los Muchachos Observatory on La Palma, Canary Islands, Spain.

We observed the star 24 times with TRES between 2022 January 29 and 2022 April 11, achieving a typical signal-to-noise ratio of 30 per resolution element. We reduced the spectra and extracted RVs following procedures outlined in L. A. Buchhave et al. (2010) and corrected for instrumental drift using an ensemble of standard stars, as in S. N. Quinn et al. (2014), achieving a typical velocity precision of about $20\,\mathrm{m\,s^{-1}}$.

We observed with NEID 20 times between 2022 March 7 and 2022 June 3. We used the high-resolution mode ($R\sim110{,}000$) and RVs were extracted using the standard NEID Data Reduction Pipeline.[61] The velocities achieved a typical precision of $\sim5\,\mathrm{m\,s^{-1}}$.

We observed with SOPHIE 12 times between 2022 February 20 and 2022 May 29, with typical exposure times of 30 minutes. We used the high-efficiency mode ($R\sim40{,}000$) with slow CCD readout, and achieved typical signal-to-noise ratios of about 14 $\mathrm{pixel^{-1}}$ at 550 nm. Instrumental stability was confirmed with standard star measurements. To extract the spectra and cross correlate them with a numerical mask, we used the pipeline described in F. Bouchy et al. (2009), and applied CCD charge transfer inefficiency corrections (F. Bouchy et al. 2013), which is particularly important for exposures with low signal-to-noise ratios. RVs were derived by cross correlation against numerical masks. We adopted results from the F0-type mask, which minimized RV dispersions and achieved a typical precision of $\sim9\,\mathrm{m\,s^{-1}}$. We also estimated and corrected for sky background contamination following the method described in D. Pollacco et al. (2008) and G. Hébrard et al. (2008).

We observed with HARPS-N 11 times between 2022 March 26 and 2023 February 3. HARPS-N is a stabilized echelle spectrograph with a resolving power of $R\sim115{,}000$ and a precision at or below the level of $1\,\mathrm{m\,s^{-1}}$ (e.g., A. Collier Cameron et al. 2021; X. Dumusque et al. 2021; Z. L. de Beurs et al. 2022; F. Lienhard et al. 2022). RVs were extracted using the HARPS-N Data Reduction Software, and achieved a typical precision of $3.5\,\mathrm{m\,s^{-1}}$.

2.4.4. TOI-5143 Stellar Parameters

We estimated the spectroscopic stellar parameters of TOI-5143 by running SPC on the TRES spectra, finding $T_{\mathrm{eff}}=5342\pm50$ K, $\log g=4.60\pm0.10$, $[\mathrm{Fe/H}]=+0.05\pm0.08$, and $v\sin i_\star=4.0\pm1.0\,\mathrm{km\,s^{-1}}$. We again caution that this estimate of the projected rotational velocity may be affected by systematic errors at a level beyond the quoted uncertainty. In this case, we can also run SPC on the HARPS-N spectra, which more robustly resolve the narrow lines and should provide a less biased measurement of the rotation. Analysis of the HARPS-N spectra did yield a slightly slower rotation of $v\sin i_\star=2.1\pm0.6\,\mathrm{km\,s^{-1}}$. We found good agreement with the other stellar parameters from TRES: $T_{\mathrm{eff}}=5316\pm50$ K, $\log g=4.50\pm0.10$, and $[\mathrm{Fe/H}]=-0.04\pm0.08$. The TESS light curve of TOI-5143 shows a hint of variation with a period close to 13 days, which would suggest an equatorial rotational velocity of $3.3\,\mathrm{km\,s^{-1}}$ if the stellar spin were aligned with the planetary orbits. The measured $v\sin i_\star$ would therefore seem to imply a modest spin–orbit misalignment, but given the uncertainty in these measurements and the potential for systematics to appear in the photometry on the timescale of the spacecraft orbit (13.7 days), such a conclusion requires more evidence.

3. EXOFASTv2 Global Fit

To understand the full system parameters and place TOI-2494 and TOI-5143 in context with the known exoplanet population, we globally modeled the available observations using the exoplanet fitting suite EXOFASTv2 (J. Eastman et al. 2013; J. D. Eastman et al. 2019). To constrain the host

[61] https://neid.ipac.caltech.edu/docs/NEID-DRP

Table 4
Stellar and Planetary Properties

Priors:		TOI-2494		TOI-5143	
Gaussian	π Gaia parallax (mas)	6.543 ± 0.045		5.5153 ± 0.0717	
Gaussian	[Fe/H] metallicity (dex)	0.06 ± 0.09		0.20 ± 0.08	
Upper limit	V-band extinction A_V (mag)	2.25		0.08	
Gaussian[a]	Dilution in TESS D_T	0.00000 ± 0.00063		0.00000 ± 0.000042	
Parameter	**Units**	**Values**		**Values**	
	Stellar Parameters:				
M_*	Mass ($M_\odot$)	$0.897^{+0.046}_{-0.041}$		$0.888^{+0.038}_{-0.037}$	
R_*	Radius ($R_\odot$)	$0.883^{+0.026}_{-0.025}$		$0.848^{+0.026}_{-0.025}$	
L_*	Luminosity ($L_\odot$)	$0.636^{+0.062}_{-0.048}$		$0.491^{+0.020}_{-0.019}$	
$F_{\rm Bol}$	Bolometric flux (cgs) $\times 10^{-9}$	$0.870^{+0.084}_{-0.065}$		0.481 ± 0.015	
ρ_*	Density (cgs)	$1.84^{+0.18}_{-0.16}$		$2.06^{+0.20}_{-0.18}$	
$\log g$	Surface gravity (cgs)	4.500 ± 0.030		$4.530^{+0.029}_{-0.030}$	
$T_{\rm eff}$	Effective temperature (K)	5490^{+130}_{-120}		5246^{+77}_{-76}	
[Fe/H]	Metallicity (dex)	$0.079^{+0.081}_{-0.072}$		$0.191^{+0.079}_{-0.078}$	
Age	Age (Gyr)	$7.2^{+3.9}_{-3.7}$		$6.9^{+4.0}_{-3.6}$	
EEP[b]	Equal evolutionary phase (EEP)	352^{+31}_{-18}		346^{+25}_{-19}	
A_V	V-band extinction (mag)	$0.19^{+0.12}_{-0.11}$		$0.047^{+0.024}_{-0.030}$	
$\sigma_{\rm SED}$	SED photometry error scaling	$0.87^{+0.36}_{-0.22}$		$1.72^{+0.71}_{-0.42}$	
ϖ	Parallax (mas)	6.540 ± 0.045		5.533 ± 0.071	
d	Distance (pc)	$152.9^{+1.1}_{-1.0}$		180.7 ± 2.3	
	Planetary Parameters:	**TOI-2494 b**	**TOI-2494 c**	**TOI-5143 b**	TOI-5143 c
P	Period (days)	$2.4087783^{+0.0000099}_{-0.0000089}$	8.3761356 ± 0.0000053	$2.3843468^{+0.0000080}_{-0.0000076}$	$5.2097090^{+0.0000034}_{-0.0000033}$
$R_{\rm P}$	Radius ($R_\oplus$)	$2.31^{+0.13}_{-0.12}$	$9.64^{+0.43}_{-0.36}$	$2.87^{+0.15}_{-0.14}$	$32.3^{+15}_{-9.5}$
$M_{\rm P}$	Mass ($M_\oplus$)	1 ± 14	82 ± 19	$8.4^{+9.4}_{-9.3}$	201 ± 14
$M_{\rm P,pred}$[c]	Predicted mass ($M_\oplus$)	6.0	⋯	8.7	⋯
$T_{\rm C}$	Time of conjunction (BJD$_{\rm TDB}$)	$2224.8498^{+0.0010}_{-0.0013}$	$2210.73182^{+0.00035}_{-0.00036}$	2526.7693 ± 0.0012	$2527.24322^{+0.00022}_{-0.00023}$
a	Semimajor axis (au)	$0.03392^{+0.00057}_{-0.00052}$	$0.0779^{+0.0013}_{-0.0012}$	$0.03357^{+0.00048}_{-0.00047}$	0.05654 ± 0.00080
i	Inclination (deg)	$86.64^{+0.57}_{-0.50}$	$87.31^{+0.15}_{-0.16}$	$87.18^{+0.75}_{-0.64}$	$84.91^{+0.57}_{-0.89}$
e	Eccentricity	⋯	$0.048^{+0.059}_{-0.034}$	⋯	$0.070^{+0.034}_{-0.033}$
ω_*	Argument of periastron (deg)	⋯	-160 ± 120	⋯	112^{+26}_{-23}
$T_{\rm eq}$	Equilibrium temperature (K)	1349^{+30}_{-25}	890^{+20}_{-17}	1271^{+15}_{-14}	979 ± 11
K	RV semiamplitude (m s^{-1})	$0.7^{+7.4}_{-6.9}$	28.0 ± 6.2	$4.4^{+4.9}_{-4.8}$	$80.4^{+5.0}_{-4.9}$
$K_{\rm pred}$[c]	Predicted RV semiamplitude (m s^{-1})	3.1	⋯	4.5	⋯
a/R_*	Semimajor axis in stellar radii	$8.26^{+0.26}_{-0.25}$	$18.97^{+0.59}_{-0.58}$	$8.52^{+0.27}_{-0.26}$	$14.35^{+0.45}_{-0.44}$
$R_{\rm P}/R_*$	Radius of planet in stellar radii	0.0240 ± 0.0010	$0.0999^{+0.0025}_{-0.0018}$	$0.0311^{+0.0011}_{-0.0010}$	$0.35^{+0.16}_{-0.10}$
δ	$(R_{\rm P}/R_*)^2$	0.000574 ± 0.000049	$0.00998^{+0.00052}_{-0.00035}$	$0.000964^{+0.000066}_{-0.000064}$	$0.122^{+0.14}_{-0.061}$
δ_B	Transit depth in B (fraction)	⋯-	⋯-	$0.001463^{+0.00010}_{-0.000098}$	$0.0024^{+0.0016}_{-0.0018}$
δ_R	Transit depth in R (fraction)	$0.000690^{+0.000061}_{-0.000060}$	$0.00774^{+0.00036}_{-0.00039}$	⋯-	⋯-
$\delta_{g'}$	Transit depth in g' (fraction)	$0.000776^{+0.000068}_{-0.000067}$	$0.00607^{+0.00043}_{-0.00051}$	$0.001350^{+0.000088}_{-0.000086}$	$0.0058^{+0.0011}_{-0.0012}$
$\delta_{i'}$	Transit depth in i' (fraction)	0.000663 ± 0.000056	$0.00826^{+0.00026}_{-0.00024}$	$0.001168^{+0.000073}_{-0.000072}$	$0.01121^{+0.00046}_{-0.00048}$
$\delta_{r'}$	Transit depth in r' (fraction)	$0.000689^{+0.000059}_{-0.000058}$	$0.00775^{+0.00024}_{-0.00025}$	$0.001205^{+0.000076}_{-0.000074}$	$0.01010^{+0.00059}_{-0.00063}$
$\delta_{z'}$	Transit depth in z' (fraction)	0.000650 ± 0.000055	$0.00852^{+0.00027}_{-0.00024}$	$0.001130^{+0.000074}_{-0.000072}$	$0.01232^{+0.00060}_{-0.00064}$
$\delta_{\rm TESS}$	Transit depth in TESS (fraction)	$0.000658^{+0.000056}_{-0.000055}$	$0.00835^{+0.00021}_{-0.00019}$	$0.001198^{+0.000075}_{-0.000074}$	$0.01033^{+0.00066}_{-0.00070}$
τ	Ingress/egress transit duration (days)	$0.00256^{+0.00023}_{-0.00022}$	$0.0369^{+0.0090}_{-0.0045}$	$0.00307^{+0.00030}_{-0.00026}$	$0.03426^{+0.00029}_{-0.00028}$
T_{14}	Total transit duration (days)	$0.0840^{+0.0020}_{-0.0018}$	0.0910 ± 0.0015	$0.0845^{+0.0020}_{-0.0026}$	$0.06851^{+0.00058}_{-0.00057}$
b	Transit impact parameter	$0.484^{+0.057}_{-0.072}$	$0.8918^{+0.010}_{-0.0090}$	$0.418^{+0.083}_{-0.10}$	$1.20^{+0.18}_{-0.12}$
$b_{\rm S}$	Eclipse impact parameter	⋯	$0.0916^{+0.0048}_{-0.0068}$	⋯	$1.34^{+0.26}_{-0.15}$
$\tau_{\rm S}$	Ingress/egress eclipse duration (days)	⋯	$0.0332^{+0.010}_{-0.0091}$	⋯	$0.0065^{+0.022}_{-0.0065}$
$T_{\rm S,14}$	Total eclipse duration (days)	⋯	$0.0916^{+0.0048}_{-0.0068}$	⋯	$0.013^{+0.044}_{-0.013}$
$\delta_{\rm S,2.5\,\mu m}$	Blackbody eclipse depth at 2.5 μm (ppm)	$15.2^{+1.8}_{-1.6}$	$29.3^{+3.9}_{-3.1}$	$21.0^{+2.0}_{-1.8}$	690^{+790}_{-340}
$\delta_{\rm S,5.0\,\mu m}$	Blackbody eclipse depth at 5.0 μm (ppm)	$53.3^{+5.2}_{-5.0}$	284^{+23}_{-18}	$81.7^{+6.7}_{-6.2}$	5000^{+5600}_{-2500}
$\delta_{\rm S,7.5\,\mu m}$	Blackbody eclipse depth at 7.5 μm (ppm)	$76.5^{+7.2}_{-6.9}$	550^{+37}_{-29}	$120.8^{+9.6}_{-8.9}$	8800^{+9900}_{-4400}
$\rho_{\rm P}$	Density (cgs)	$0.6^{+6.5}_{-6.1}$	$0.50^{+0.14}_{-0.13}$	$1.9^{+2.2}_{-2.1}$	$0.033^{+0.061}_{-0.022}$
$\log g_{\rm P}$	Surface gravity	$3.27^{+0.33}_{-0.53}$	$2.936^{+0.097}_{-0.12}$	$3.10^{+0.26}_{-0.43}$	$2.28^{+0.30}_{-0.33}$
$\langle F \rangle$	Incident flux (10^9 erg s^{-1} cm^{-2})	$0.753^{+0.069}_{-0.054}$	$0.142^{+0.013}_{-0.010}$	$0.592^{+0.028}_{-0.026}$	$0.2076^{+0.0093}_{-0.0089}$
$T_{\rm P}$	Time of periastron (BJD$_{\rm TDB}$)	$2224.8496^{+0.0010}_{-0.0013}$	$2204.2^{+2.7}_{-3.1}$	2526.7691 ± 0.0012	$2522.31^{+0.35}_{-0.28}$
$T_{\rm S}$	Time of eclipse (BJD$_{\rm TDB}$)	$2226.0538^{+0.0010}_{-0.0013}$	$2214.91^{+0.27}_{-0.33}$	2525.5769 ± 0.0012	$2529.770^{+0.080}_{-0.088}$
$T_{\rm A}$	Time of ascending node (BJD$_{\rm TDB}$)	$2226.6562^{+0.0010}_{-0.0013}$	$2208.63^{+0.15}_{-0.21}$	2528.5573 ± 0.0012	$2526.001^{+0.071}_{-0.063}$
$T_{\rm D}$	Time of descending node (BJD$_{\rm TDB}$)	$2225.4518^{+0.0010}_{-0.0013}$	$2212.82^{+0.18}_{-0.17}$	2527.3652 ± 0.0012	$2523.199^{+0.072}_{-0.070}$

Table 4
(Continued)

Priors:		TOI-2494		TOI-5143	
$e\cos\omega_*$	...	...	$-0.002^{+0.050}_{-0.061}$	...	$-0.023^{+0.024}_{-0.026}$
$e\sin\omega_*$	...	...	$-0.004^{+0.030}_{-0.040}$	...	0.060 ± 0.035
M_P/M_*	Mass ratio	$0.5^{+4.8}_{-4.5} \times 10^{-5}$	0.000276 ± 0.000062	$2.8^{+3.2}_{-3.2} \times 10^{-5}$	$6.82^{+0.43}_{-0.42} \times 10^{-4}$

Notes. See Table 3 in J. D. Eastman et al. (2019) for a detailed description of all derived and fitted parameters. We report the median values and 68% confidence intervals.
[a] We assume the TESS correction for blending is much better than 10%. We use a prior of 10% of the determined blending from TIC v.8 (K. G. Stassun et al. 2018).
[b] The EEP corresponds to static points in a star's evolutionary history when using the MIST isochrones and can be a proxy for age. See Section 2 in A. Dotter (2016) for a more detailed description of the EEP.
[c] Predicted masses are based on the median measured radii and the J. Chen & D. Kipping (2017) mass–radius relation, though we stress that planets of this size span a wide range of densities, and the actual masses could differ by a large factor.

star parameters within the global analysis, we simultaneously fit each spectral energy distribution (SED) using the broadband photometry shown in Table 1 and the MESA Isochrones and Stellar Tracks (MIST) stellar evolution models (B. Paxton et al. 2011, 2013, 2015; J. Choi et al. 2016; A. Dotter 2016), with Gaussian priors on the host star metallicity ([Fe/H]) derived from spectroscopy and on the parallax from Gaia DR2 (Gaia Collaboration et al. 2018; all user priors and limits are shown at the top of Table 4). For the SED portion of the fit, we adopted a lower limit of 3% on the bolometric flux systematic uncertainty as well as lower limits on the systematic uncertainties of the broadband photometric measurements (shown in Table 1). To model the planets within each system, we fit the TESS and SG1 transits (see Figure 1) and the extracted RVs from TRES, FEROS, CHIRON, NEID, SOPHIE, and HARPS-N (see Section 2.4). We determined convergence based on the EXOFASTv2 suggestion for the Gelman–Rubin statistic (<1.01) and independent draws (>1000). See Tables 4 and 5 and Figures 2 and 4 for the final global fit results.

3.1. Review of TOI-2494 and TOI-5143

TOI-2494 c and TOI-5143 c belong to the category of close-orbiting giant planets accompanied by inner small planets, of which fewer than a dozen are known. TOI-2494 is a main-sequence late G dwarf located at a distance of 152.9 ± 1.1 pc with a mass of $0.911^{+0.051}_{-0.045}\,M_\odot$, a radius of $0.901^{+0.036}_{-0.033}\,R_\odot$, an effective temperature of 5430^{+140}_{-130} K, and a slightly super-solar metallicity ($[\mathrm{Fe/H}] = 0.095^{+0.085}_{-0.077}$ dex). It hosts a mini-Neptune ($2.35^{+0.16}_{-0.15}\,R_\oplus$) at a period of 2.41 days and a large ($R_P = 21.4^{+2.4}_{-4.1}\,R_\oplus$) Saturn-mass ($M_P = 80 \pm 18\,M_\oplus$) planet orbiting on a 8.38 day period. TOI-5143 is also a main-sequence late G dwarf ($T_{\mathrm{eff}} = 5289^{+81}_{-83}$ K), with a mass of $0.913^{+0.037}_{-0.040}\,M_\odot$ and a radius of $0.835^{+0.027}_{-0.025}\,R_\odot$. The star exhibits some metal enrichment ($[\mathrm{Fe/H}] = 0.191^{+0.078}_{-0.079}$ dex) and sits at a distance of 180.7 pc. TOI-5143 also hosts a short-period (2.38 days) mini-Neptune ($2.73^{+0.19}_{-0.17}\,R_\oplus$) and an outer (5.21 days) hot Jupiter ($R_\star = 31.4^{+14}_{-9.0}\,R_\oplus$) with a mass of $208 \pm 14\,M_\oplus$. Both TOI-2494 c and TOI-5143 c, the two close-in giant planets, reside in grazing configurations relative to our line of sight ($b = 1.066^{+0.028}_{-0.053}$ and $1.19^{+0.16}_{-0.11}$, respectively), resulting in a poor constraint on the measured planetary radii from our EXOFASTv2 global analysis (see Section 3). We see no evidence of any significant eccentricity in either system's orbit, but this is not surprising given their compact architectures.

3.2. Validation of the Small, Inner Planets

Our RV data of TOI-2494 and TOI-5143 are not precise enough to detect the orbital motion induced by the inner companions, and we do not detect significant TTVs that might be used to confirm that each small planet orbits within the same planetary system as its nearby giant planet. Therefore, we cannot immediately confirm the planetary nature of these objects. For TOI-2494, there remains a small chance that there is a faint, unresolved stellar companion or background star that hosts a companion responsible for the shallow transits. For TOI-5143, the shallow transit events may arise from the faint, 0.″6 companion, or another undetected, unresolved star. To assess the false positive probability (FPP) of these small planets, we use the TRICERATOPS validation software (S. Giacalone et al. 2021). While we find that both objects are much more likely to be planets than not, the FPPs—6.0% for TOI-2494 b and 3.0% for TOI-5143 b—are not formally low enough that we would normally claim them to be validated planets. However, we can also assess the validity of the most likely false positive scenarios identified by TRICERATOPS by considering information not available to the code.

The most likely false positive scenarios for TOI-2494 b involve a planet orbiting a bound companion (∼3%) or an unresolved background eclipsing binary (∼3%). A blended binary host must be at most 7.1 mag fainter than the primary to reproduce the depth of the transits. Taking advantage of the proper motion of TOI-2494, we can exclude the latter scenario using archival imaging from the Palomar Observatory Sky Survey (POSS), in which no stars are visible at the present-day position of TOI-2494. The former scenario cannot be completely excluded, but it is less likely than formally calculated. In particular, multiband ground-based photometry does not detect a chromatic dependence of the transit depth, and some fraction of the bound companions that remain undetected in high-resolution imaging would be expected to induce astrometric noise, but Gaia DR3 shows no evidence of a nearby star (renormalized unit weight error (RUWE) = 1.00). Similar arguments apply to TOI-5143, though its proper motion is a little smaller, which makes its present-day position slightly blended with the PSF of archival POSS images. This is somewhat offset by the deeper transit of TOI-5143 b, which requires a star with a magnitude difference less than 6.6. Gaia DR3 shows no unexplained astrometric noise (RUWE = 0.82).

These considerations will push the FPPs closer to the TRICERATOPS-recommended validation threshold of FPP < 0.015, and we proceed under the assumption that TOI-2494 b and TOI-5143 b are planets. Nevertheless, we

Table 5
Observational Parameters

Parameter		Values					
TOI-2494							
Wavelength Parameters:		*R*	*g*’	*i*’	*r*’	*z*’	TESS
u_1	Linear limb-darkening coeff.	0.438 ± 0.056	$0.658^{+0.045}_{-0.047}$	0.355 ± 0.036	$0.438^{+0.036}_{-0.037}$	$0.310^{+0.038}_{-0.039}$	$0.339^{+0.038}_{-0.039}$
u_2	Quadratic limb-darkening coeff.	0.259 ± 0.052	0.152 ± 0.041	0.251 ± 0.031	0.233 ± 0.030	0.271 ± 0.035	0.244 ± 0.035
Telescope Parameters:		CHIRON	FEROS	TRES			
$\gamma_{\rm rel}$	Relative RV offset (m s^{-1})	$-23445.7^{+4.6}_{-4.7}$	−24056 ± 21	24 ± 37			
σ_J	RV jitter (m s^{-1})	$0.00^{+8.9}_{-0.00}$	41^{+42}_{-17}	72^{+78}_{-32}			
σ_J^2	RV jitter variance	-110^{+190}_{-110}	1700^{+5300}_{-1100}	5200^{+18000}_{-3600}			
Transit Parameters:		TESS S6	TESS S33 (TESS)	KepCam 2021-03-04 (*i*’)	El Sauce 2021-03-20 (*R*)	LCO-CTIO 2021-10-02 (*i*’)	
CHAT 2021-10-15 (*r*’)	CHAT 2021-11-26 (*r*’)	MuSCAT2 2022-01-13 (*g*’)	MuSCAT2 2022-01-13 (*i*’)	MuSCAT2 2022-01-13 (*r*’)	MuSCAT2 2022-01-13 (*z*’)		
DragonFly 2022-03-16 (*g*’)	DragonFly 2022-03-16 (*r*’)	LCO-SSO UT 2022-12-17 (*g*’)	LCO-SSO UT 2022-12-17 (*z*’)				
σ^2	Added variance	$0.2^{+1.8}_{-1.6} \times 10^{-8}$	$-4.2^{+5.7}_{-5.5} \times 10^{-8}$	$1.139^{+0.097}_{-0.087} \times 10^{-5}$	$1.86^{+0.66}_{-0.56} \times 10^{-7}$	$4.10^{+0.47}_{-0.41} \times 10^{-6}$	
$6.31^{+1.0}_{-0.90} \times 10^{-6}$	$-0.78^{+1.1}_{-0.92} \times 10^{-6}$	$0.0^{+4.9}_{-4.5} \times 10^{-7}$	$0.4^{+4.9}_{-4.6} \times 10^{-7}$	$9.7^{+6.4}_{-6.0} \times 10^{-7}$	$6.0^{+5.6}_{-5.2} \times 10^{-7}$		
$1.73^{+0.24}_{-0.20} \times 10^{-5}$	$9.4^{+1.3}_{-1.1} \times 10^{-6}$	$1.18^{+0.36}_{-0.30} \times 10^{-6}$	$1.10^{+0.38}_{-0.32} \times 10^{-6}$				
F_0	Baseline flux	$1.000061^{+0.000031}_{-0.000030}$	1.000005 ± 0.000029	1.00261 ± 0.00021	0.205336 ± 0.000064	1.00010 ± 0.00014	
0.99843 ± 0.00021	0.99907 ± 0.00028	1.00019 ± 0.00013	1.00004 ± 0.00012	0.99871 ± 0.00013	$0.99868^{+0.00014}_{-0.00013}$		
0.99840 ± 0.00036	1.00032 ± 0.00028	1.00032 ± 0.00017	$1.00034^{+0.00018}_{-0.00017}$				
C_0	Additive detrending coeff.	…	…	$-0.00609^{+0.00051}_{-0.00050}$	−0.00022 ± 0.00075	−0.00126 ± 0.00038	
…	…	…	…	…	…		
−0.00043 ± 0.00083	0.00146 ± 0.00065	…	…				
A_D	Dilution from neighboring stars	$-0.00000^{+0.00045}_{-0.00044}$	$-0.00000^{+0.00045}_{-0.00044}$	…	…	…	
…	…	…	…	…	…		
…	…	…	…				
TOI-5143							
Wavelength Parameters:		*B*	*g*’	*i*’	*r*’	*z*’	TESS
u_1	Linear limb-darkening coeff.	$0.791^{+0.050}_{-0.051}$	0.671 ± 0.044	0.420 ± 0.029	0.479 ± 0.034	$0.356^{+0.040}_{-0.041}$	$0.467^{+0.038}_{-0.039}$
u_2	Quadratic limb-darkening coeff.	$-0.003^{+0.052}_{-0.051}$	0.039 ± 0.047	$0.239^{+0.028}_{-0.027}$	0.179 ± 0.034	0.264 ± 0.043	0.247 ± 0.041
A_D	Dilution from neighboring stars	…	…	…	…	…	0.0 ± 0.00042
Telescope Parameters:		HARPS-N	NEID	SOPHIE	TRES		
$\gamma_{\rm rel}$	Relative RV offset (m s^{-1})	−52 ± 12	13427.6 ± 4.5	$13238.9^{+5.6}_{-5.9}$	$90.8^{+6.5}_{-6.3}$		
σ_J	RV jitter (m s^{-1})	$36.5^{+12}_{-8.1}$	$18.7^{+4.3}_{-3.2}$	$17.1^{+8.0}_{-5.9}$	$16.9^{+9.3}_{-11}$		
σ_J^2	RV jitter variance	1330^{+1100}_{-530}	350^{+180}_{-110}	290^{+340}_{-170}	290^{+400}_{-250}		
Transit Parameters:		TESS	MuSCAT2 2022-01-31 (*g*’)	MuSCAT2 2022-01-31 (*i*’)	MuSCAT2 2022-01-31 (*r*’)	MuSCAT2 2022-01-31 (*z*’)	

Table 5
(Continued)

Parameter		Values				
PEST 2022-02-15 (r')	KepCam 2022-04-19 (B)	KepCam 2022-04-19 (i')	LCO-SAAO 2022-05-04 (i')			
σ^2	Added variance	$-1.736^{+0.067}_{-0.066} \times 10^{-6}$	$8.1^{+1.9}_{-1.7} \times 10^{-7}$	$6.4^{+3.8}_{-3.6} \times 10^{-7}$	$4.7^{+1.6}_{-1.5} \times 10^{-7}$	$5.8^{+4.9}_{-4.5} \times 10^{-7}$
$1.12^{+0.27}_{-0.23} \times 10^{-5}$	$1.69^{+0.25}_{-0.21} \times 10^{-5}$	$0.000185^{+0.000023}_{-0.000019}$	$1.81^{+0.20}_{-0.18} \times 10^{-5}$			
F_0	Baseline flux	1.000014 ± 0.000026	1.00005 ± 0.00011	1.00016 ± 0.00011	$1.000076^{+0.000097}_{-0.000098}$	1.00006 ± 0.00013
0.99934 ± 0.00038	$1.00203^{+0.00036}_{-0.00035}$	1.0015 ± 0.0010	1.00003 ± 0.00030			
C_0	Additive detrending coeff.	…	…	…	…	…
0.0008 ± 0.0012	0.0020 ± 0.0011	−0.0116 ± 0.0032	−0.0030 ± 0.0013	...	...	...

recommend continued monitoring with precise RVs and transit photometry to measure the masses and/or detect TTVs to confirm their planetary nature and better characterize the planetary systems. Additional transit photometry may also improve the determination of the transit shapes and reduce the formal FPPs to allow more confident validation.

4. Discussion

4.1. Are Hot Jupiters Closely Aligned with Their Friends?

One striking result from the Kepler survey was that transiting hot Jupiters tend to be lonely (J. H. Steffen et al. 2012). That is, there is no evidence in the transit data that hot Jupiters commonly exist in compact multiplanet systems, which are so common for small planets—hot Jupiters do not often have "close friends." Very recently, L. Sha et al. (2026) used the first 5 yr of TESS data to determine that only $7.6\%^{+5.5\%}_{-3.8\%}$ of hot Jupiter systems host additional close transiting planetary companions. Now, thanks to the growing number of these systems discovered by TESS, we can begin to examine the characteristics of the population and, by extension, uncover details about the formation channel that produces them. For example, one might ask whether the mutual orbital inclinations of hot Jupiters and their close friends are similar to the mutual inclinations seen in other populations. If the characteristic mutual inclinations of a population are sculpted by formation and dynamical interactions, then we can potentially learn about the origins of these hot Jupiters with close friends by comparing their mutual inclinations to those of other populations.

One hypothesis is that these hot Jupiters with close friends are the short-period tail of the warm Jupiter population, in which close planetary companions are not rare (C. Huang et al. 2016; D.-H. Wu et al. 2023). It would therefore be natural to compare the two populations to see if they are consistent. However, simple geometric arguments dictate that transiting warm Jupiters in multiplanet systems must have a narrower range of mutual inclinations than hot Jupiters, so we cannot directly compare the two. Moreover, the difference in semimajor axes between hot and warm Jupiters may lead to differences in mutual inclinations driven by postformation interactions with the host star and disk (see, e.g., C. Spalding & K. Batygin 2017). Obliquity measurements of hot and warm Jupiter host stars (e.g., J. Dong et al. 2023; A. Bieryla et al. 2024) are more likely to yield a fruitful comparison of the angular momentum components in these populations.

One could instead compare hot Jupiter systems to short-period systems of small planets spanning a similar range of orbital separations. It has been established that systems of small planets tend to have low mutual inclinations (with a mode between 1° and $2\overset{\circ}{.}2$; D. C. Fabrycky et al. 2014; see also S. Tremaine & S. Dong 2012). This provides a benchmark for comparison to the hot Jupiters with close friends. However, we must be cognizant of differences that remain between the two samples.

F. Dai et al. (2018) showed that planets very close to their host star (within about 5 R_*) may have experienced inclination excitation. These most extreme inner planets also tend to have larger period ratios with the next closest planet, which makes them susceptible to other sources of mutual inclination excitation. For example, J. Becker et al. (2020) demonstrate that it is possible to incline outer planets relative to an ultrashort-period inner planet through interaction with a much more distant, massive companion. While it is possible that some inner planets in hot Jupiter systems could be impacted by these processes, most of the close friends of hot Jupiters orbit beyond 5 R_* and none have particularly large period ratios, so the mechanisms that excite mutual inclinations in ultrashort-period planetary systems are likely to be different from those that affect the hot Jupiters.

Of more relevance to the hot Jupiters with close friends, S. C. Millholland et al. (2021) find evidence that the mutual inclination distribution of small planets varies inversely with the number of planets in the system, such that two-planet systems have a mean mutual inclination of a few degrees, while five-planet systems are typically mutually inclined by only 1° (see also W. Zhu et al. 2018). A comparison between hot Jupiters and small planets should therefore carefully consider which subsample of small planets is most appropriate to minimize dynamical differences in the environments.

Finally, we note that determination of the mutual inclination distribution of small planets relies upon the robust sample of hundreds of systems. We are not afforded that luxury for hot Jupiters with close friends. Instead, we use a measure of the minimum possible mutual inclination for each system: the differences in line-of-sight inclinations derived from transit modeling. The observed distribution of this minimum mutual inclination for the seven hot Jupiters with close friends peaks at low values, apparently near 0°, and typically less than about 3° (see Figure 5).

There is of course an ambiguity regarding the hemisphere across which each planet transits. If we assume a tendency toward alignment, with both planets transiting the same hemisphere, the distribution peaks at 0°, with 68.3% of planet pairs aligned within $3\overset{\circ}{.}1$ (solid blue line in Figure 5). If the hemisphere of transit is drawn randomly, the distribution is of course broader, still peaking near 0°, but with a 68.3% of pairs within $6\overset{\circ}{.}1$ (dashed light blue line). As noted above, these are minimum mutual inclinations, so we calculate the same quantities for known small planets to make a fair comparison. To match the characteristics of the hot Jupiter sample and minimize the impact of dynamical effects that do not also operate in hot Jupiter systems, we select only the 195 systems with two small transiting planets orbiting with periods shorter than 10 days. We note that the stellar samples match quite well, with the vast majority of these planets orbiting G stars similar to most of the hot Jupiter hosts (i.e., orange to yellow in the top panel of Figure 5). The resulting mutual inclination distributions, also shown in Figure 5 (as orange lines), are quite similar to those of the hot Jupiter systems. They peak at 0°, as expected, with 68.3% of systems within $2\overset{\circ}{.}6$ when assuming a tendency toward alignment, and $4\overset{\circ}{.}0$ for randomly drawn transit hemispheres. A Kolmogorov–Smirnov test cannot reject the null hypothesis that the two populations are drawn from the same distribution: using the one-hemisphere distributions (illustrated by the solid lines in Figure 5), the p-value is 0.376. This of course does not prove that the two populations formed in the same way, but it fails to reject the hypothesis; to within the precision of these measurements, hot Jupiters with close friends and the much more common small planet systems display similar levels of orbital angular momentum misalignment. If there are any differences in their origins, those processes must broadly preserve—or produce—this orbital alignment.

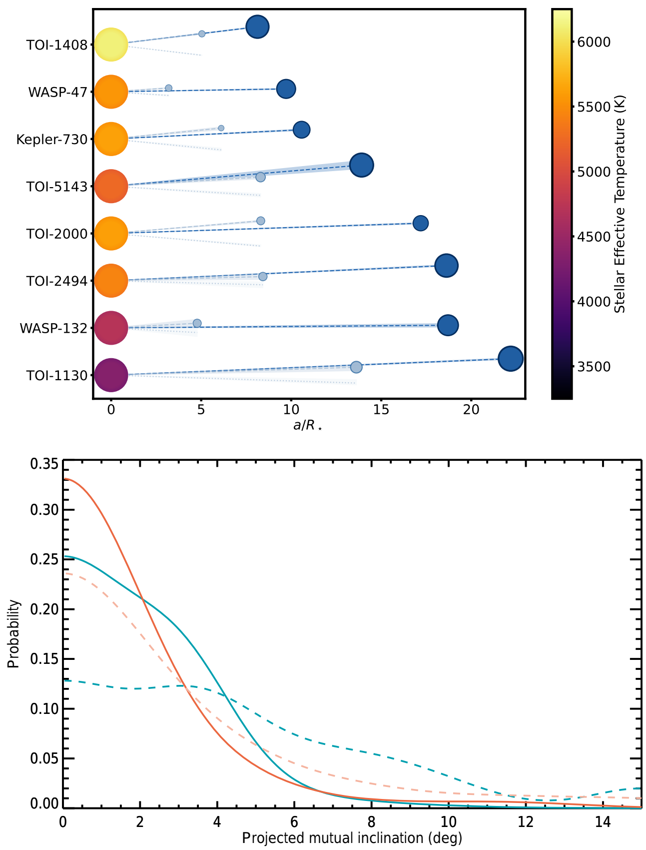

Figure 5. Top: a schematic showing the inclinations of hot Jupiters and their interior small companions. Each host star is colored by its effective temperature. The orbital distances and impact parameters are to scale, but the planet sizes have been increased for visibility. Dashed lines and shaded regions indicate the orientation of the orbital planes, with outer giant planets shown in dark blue and inner small planets shown in light blue. Note that the hemisphere across which the planets transit cannot be determined, which we illustrate by plotting the two possible relative positions of the inner orbits—i.e., on the same or opposite hemisphere as the giant planets. Bottom: the distribution of the minimum mutual inclinations illustrated in the top panel (blue lines), smoothed using kernel density estimation, assuming (a) no preference for the hemisphere over which the planets transit (dashed line); or (b) that the planets transit the same hemisphere (solid line). The equivalent distributions of minimum mutual inclinations of small planet systems containing two transiting planets with periods shorter than 10 days are plotted in orange.

4.2. Hot Jupiters with Companions as a Key for Decoding Giant Planet Migration

One way to measure the prevalence of different evolutionary pathways is to identify planetary systems that must have been produced by a specific mechanism, and use the properties of those keystone systems to infer the evolutionary histories of the broader population. Many factors impede this approach. For example, the primordial imprints of HEM can be erased by tidal circularization and obliquity damping, and ongoing dynamical evolution can disrupt the hallmark orbital architectures of in situ formation or disk migration. A first step is to differentiate between systems that must have experienced dynamically cold evolution (disk migration or in situ formation) and those that likely have a dynamically hot history (high-eccentricity tidal migration). Hot Jupiters with close friends represent a population that could not have migrated on highly eccentric orbits, given the presence of their nearby inner companions that would have been disrupted during HEM when the giant planets' initial periastron distances were one-half of their current distances. If these systems all bear a signature unique to their dynamically quiet formation channel, it can be used to identify other systems that formed that way, whether or not they have inner companions.

The carbon-to-oxygen ratio (C/O) of a planet's atmosphere has been proposed as such a marker, as C/O is expected to vary throughout the protoplanetary disk (K. I. Öberg et al. 2011; N. Madhusudhan et al. 2014). Beyond the water ice line, a significant amount of oxygen should be sequestered in ices, depleting oxygen in the gas phase and therefore raising the C/O of the gas from which giant planet atmospheres are accreted. Therefore, if a giant planet forms interior to the water ice line (e.g., via in situ hot Jupiter formation), its atmospheric C/O should be low, and if it originates beyond the ice line (as is typically assumed for core accretion formation), its C/O should be high.

This picture is only a first-order approximation, as highlighted by ongoing work to build models that properly account for more complex accretion, entrapment, and sublimation behaviors. If a planet undergoes disk-driven migration starting from beyond the ice line, the planet may accrete gas during migration from a range of orbital separations, potentially resulting in an intermediate C/O. Significant pebble accretion during disk migration could also affect both metallicity and C/O (N. Madhusudhan et al. 2014; C. Mordasini et al. 2016), and entrapment of CO in water ices may provide a means to enrich C inside the water ice line (J. Williams et al. 2025). A robust sample of planets will therefore be needed to help interpret what will likely be a somewhat murkier result. Nevertheless, knowing the evolutionary history of a specific system may allow us to identify a combination of molecular ratios in its atmosphere that are indicative of that evolutionary history. The unusual architectures of TOI-2494 and TOI-5143 mark them, along with the small handful of previously known hot Jupiters with friends (J. C. Becker et al. 2015; C. I. Cañas et al. 2019; C. X. Huang et al. 2020a; B. J. Hord et al. 2022; G. Maciejewski et al. 2023; L. Sha et al. 2023; J. Korth et al. 2024), as examples of systems that have undergone a dynamically quiet migration history.

Similarly, it is possible to identify systems that cannot be explained by a dynamically quiet evolutionary history, which are suggestive of formation beyond the ice line followed by multibody dynamical interactions leading to tidal migration. Examples of systems that represent the dynamically hot sample would be hot and warm Jupiters with high eccentricities like TOI-3362 b ($e = 0.815$, $P = 18.1$ days; J. Dong et al. 2021), TIC 237913194 b ($e = 0.575$, $P = 15.17$ days; M. Schlecker et al. 2020), Kepler-75 b ($e = 0.570$, $P = 8.88$ days; A. S. Bonomo et al. 2015), and CoRoT-10 b ($e = 0.53$, $P = 13.24$ days; A. S. Bonomo et al. 2010); or highly eccentric planets with longer periods like HD 80606 b ($e = 0.93$, $P = 111.4$ days; D. Naef et al. 2001; C. Moutou et al. 2009) and TIC 241249530 b ($e = 0.94$, $P = 165.8$ days; A. F. Gupta et al. 2024), which are probably destined to become hot Jupiters via tidal friction.

Precise transmission spectroscopy of these distinct populations, e.g., with JWST, may reveal benchmark atmospheric characteristics tied to each formation channel, which can be used to infer likely evolutionary histories from other giant planet transmission spectra. We expect this to be particularly fruitful when ESA's ARIEL mission performs transmission spectroscopy for hundreds of warm and hot giant planets (G. Tinetti et al. 2018); the chemical signatures imprinted on planetary atmospheres during formation can be decoded using the key provided by hot Jupiters with friends.

5. Conclusion

In this work we present the discovery and characterization of two new hot Jupiter systems that have small, inner companions. TOI-2494 b is a mini-Neptune on a 2.41 day period interior to the hot Jupiter TOI-2494 c ($P = 8.38$ days). The mini-Neptune TOI-5143 b resides on a 2.38 day period interior to the hot Jupiter TOI-5143 c ($P = 5.21$ days). We measure the masses of the hot Jupiters to be $80 \pm 19\,M_\oplus$ for TOI-2494 c and $201 \pm 14\,M_\oplus$ for TOI-5143 c. We note that both hot Jupiters reside in grazing configurations (impact parameters of $1.066^{+0.028}_{-0.053}$ for TOI-2494 c and $1.20^{+0.18}_{-0.12}$ for TOI-5143 c), limiting our ability to precisely measure their radii, but leading us to investigate the mutual inclinations of the population of hot Jupiters with small inner companions. We find preliminary evidence that the mutual inclinations are typically low, similar to the Kepler small planets, which are not expected to have experienced significant orbital migration. TOI-2494 and TOI-5143 join a small sample of known hot Jupiter systems that are flanked by small planets. This orbital architecture is indicative of a dynamically quiet migration history, possibly even forming in situ, and identifies these as keystone systems that can be used to anchor the interpretation of atmospheric characterization efforts from JWST and future facilities.

Acknowledgments

The results described in this paper rely on data from the TESS mission. Funding for the TESS mission is provided by NASA's Science Mission Directorate. We acknowledge the use of public TESS data from pipelines at the TESS Science Office and TESS Science Processing Operations Center. Resources supporting this work were provided by the NASA High-End Computing (HEC) Program through the NASA Advanced Supercomputing (NAS) Division at Ames Research Center for the production of the SPOC data products. This paper includes data collected by the TESS mission, which are publicly available from the Mikulski Archive for Space Telescopes (MAST).

This research has made use of the Exoplanet Follow-up Observation Program website, which is operated by the California Institute of Technology, under contract with the National Aeronautics and Space Administration under the Exoplanet Exploration Program.

This work has made use of data from the European Space Agency (ESA) mission Gaia,[62] processed by the Gaia Data Processing and Analysis Consortium (DPAC).[63] Funding for the DPAC has been provided by national institutions, in particular the institutions participating in the Gaia Multilateral Agreement.

This work makes use of observations from the LCOGT network. Part of the LCOGT telescope time was granted by NOIRLab through the Mid-Scale Innovations Program (MSIP). MSIP is funded by NSF.

This paper is based in part on observations made with the MuSCAT3 instrument, developed by the Astrobiology Center (ABC) and under financial supports by JSPS KAKENHI (JP18H05439) and JST PRESTO (JPMJPR1775), at Faulkes Telescope North on Maui, HI, operated by the Las Cumbres Observatory. It is also based on observations made with the MuSCAT2 instrument, developed by ABC, at Telescopio Carlos Sánchez operated on the island of Tenerife by the IAC in the Spanish Observatorio del Teide. This work is partly supported by JSPS KAKENHI grant Nos. JP18H01265, and JP18H05439, and JST PRESTO grant No. JPMJPR1775.

TRAPPIST is funded by the Belgian Fund for Scientific Research (Fond National de la Recherche Scientifique, FNRS) under the grant PDR T.0120.21. E.J. is FNRS Director of Research.

Data presented were obtained by the NEID spectrograph built by Penn State University and operated at the WIYN Observatory by NSF NOIRLab (NOIRLab Proposal ID 2022A-543544; PI: S. Yee), under the NN-EXPLORE partnership of the National Aeronautics and Space Administration and the U.S. National Science Foundation. The WIYN Observatory is a joint facility of the NSF's National Optical-Infrared Astronomy Research Laboratory, Indiana University, the University of Wisconsin-Madison, Pennsylvania State University, Purdue University, and Princeton University. The authors are honored to be permitted to conduct astronomical research on Iolkam Du'ag (Kitt Peak), a mountain with particular significance to the Tohono O'odham.

We thank the Observatoire de Haute-Provence (CNRS) staff for its support. This work was supported by CNES and the "Programme National de Planétologie" (PNP) of CNRS/INSU.

We acknowledge funding from the French ANR under contract number ANR18CE310019 (SPlaSH). X.D. and T.F. acknowledge funding the Investissements d'Avenir program (ANR-15-IDEX-02), through the funding of the "Origin of Life" project of the Université Grenoble Alpes.

S.N.Q., K.A.C., and A.B. acknowledge support from the TESS mission via subaward s3449 from MIT. This work was also supported by the TESS GI Program under award 80NSSC21K1056 (G03268; PI: Quinn). C.M. would like to gratefully acknowledge the entire Dragonfly Telephoto Array team, and Bob Abraham in particular, for allowing their telescope bright time to be put to use observing exoplanets. A. P. acknowledges support from grant BK-236/RAu-11/2023. The postdoctoral fellowship of K.B. is funded by F.R.S.-FNRS grant T.0109.20 and by the Francqui Foundation. E.P. acknowledges funding from the Spanish Ministry of Economics and Competitiveness through project PGC2021-125627OB-C32. B.S.S. acknowledges the support of M.V. Lomonosov Moscow State University Program of Development. The postdoctoral fellowship of K.B. is funded by F.R.S.-FNRS grant T.0109.20 and by the Francqui Foundation. G.N. acknowledges research funding from the Ministry of Science and Higher Education program the "Excellence Initiative—Research University" conducted at the Center of Excellence in Astrophysics and Astrochemistry of the Nicolaus Copernicus University in Toruń, Poland. F.J.P. acknowledges financial support from the Severo Ochoa grant CEX2021-001131-S funded by MCIN/AEI/10.13039/501100011033 and Ministerio de Ciencia e Innovación through the project PID2022-137241NB-C43. E.M. acknowledges funding from FAPEMIG under project number APQ-02493-22 and a research

[62] https://www.cosmos.esa.int/gaia
[63] https://www.cosmos.esa.int/web/gaia/dpac/consortium

productivity grant No. 309829/2022-4 awarded by the CNPq, Brazil. This publication benefits from the support of the French Community of Belgium in the context of the FRIA Doctoral Grant awarded to MT.

Software: EXOFASTv2 (J. Eastman et al. 2013; J. D. Eastman et al. 2019), AstroImageJ (K. A. Collins et al. 2017), Tapir (E. Jensen 2013).

ORCID iDs

Samuel N. Quinn https://orcid.org/0000-0002-8964-8377
Joseph E. Rodriguez https://orcid.org/0000-0001-8812-0565
Karen A. Collins https://orcid.org/0000-0001-6588-9574
Allyson Bieryla https://orcid.org/0000-0001-6637-5401
Jiayin Dong https://orcid.org/0000-0002-3610-6953
Kyle Hixenbaugh https://orcid.org/0000-0002-8685-5397
David W. Latham https://orcid.org/0000-0001-9911-7388
Brandon T. Radzom https://orcid.org/0000-0002-0015-382X
Andrew Vanderburg https://orcid.org/0000-0001-7246-5438
Songhu Wang https://orcid.org/0000-0002-7846-6981
Samuel W. Yee https://orcid.org/0000-0001-7961-3907
George Zhou https://orcid.org/0000-0002-4891-3517
Ilaria Carleo https://orcid.org/0000-0002-0810-3747
Pia Cortés-Zuleta https://orcid.org/0000-0002-6174-4666
Thierry Forveille https://orcid.org/0000-0003-0536-4607
Davide Gandolfi https://orcid.org/0000-0001-8627-9628
Elisa Goffo https://orcid.org/0000-0001-9670-961X
Neda Heidari https://orcid.org/0000-0002-2370-0187
Eder Martioli https://orcid.org/0000-0002-5084-168X
Grzegorz Nowak https://orcid.org/0000-0002-7031-7754
Enric Palle https://orcid.org/0000-0003-0987-1593
Rafael Brahm https://orcid.org/0000-0002-9158-7315
Thomas Henning https://orcid.org/0000-0002-1493-300X
Melissa J. Hobson https://orcid.org/0000-0002-5945-7975
Andrés Jordán https://orcid.org/0000-0002-5389-3944
Chelsea X. Huang https://orcid.org/0000-0003-0918-7484
Lizhou Sha https://orcid.org/0000-0001-5401-8079
Alton Spencer https://orcid.org/0000-0001-9263-6775
Ashley Ashiku https://orcid.org/0009-0002-9034-4909
Khalid Barkaoui https://orcid.org/0000-0003-1464-9276
Zouhair Benkhaldoun https://orcid.org/0000-0001-6285-9847
Michael L. Calkins https://orcid.org/0000-0002-2830-5661
Kevin I. Collins https://orcid.org/0000-0003-2781-3207
Dennis M. Conti https://orcid.org/0000-0003-2239-0567
Gilbert A. Esquerdo https://orcid.org/0000-0002-9789-5474
Phil Evans https://orcid.org/0000-0002-5674-2404
Mourad Ghachoui https://orcid.org/0000-0003-3986-0297
Michaël Gillon https://orcid.org/0000-0003-1462-7739
Elisabeth Heldridge https://orcid.org/0009-0001-2900-7834
Keith Horne https://orcid.org/0000-0003-1728-0304
Steve B. Howell https://orcid.org/0000-0002-2532-2853
Emmanuël Jehin https://orcid.org/0000-0001-8923-488X
Christopher R. Mann https://orcid.org/0000-0002-9312-0073
Adam Popowicz https://orcid.org/0000-0003-3184-5228
Francisco J. Pozuelos https://orcid.org/0000-0003-1572-7707
Justus J. Randolph https://orcid.org/0000-0001-6733-5380
Howard M. Relles https://orcid.org/0009-0009-5132-9520
Boris Safonov https://orcid.org/0000-0003-1713-3208
Richard P. Schwarz https://orcid.org/0000-0001-8227-1020
Jonathan J. Swift https://orcid.org/0000-0002-9486-818X
Thiam-Guan Tan https://orcid.org/0000-0001-5603-6895
Mathilde Timmermans https://orcid.org/0009-0008-2214-5039
Cristilyn N. Watkins https://orcid.org/0000-0001-8621-6731
Carl Ziegler https://orcid.org/0000-0002-0619-7639
Jessie L. Christiansen https://orcid.org/0000-0002-8035-4778
Tansu Daylan https://orcid.org/0000-0002-6939-9211
Martin Paegert https://orcid.org/0000-0001-8120-7457
Eric B. Ting https://orcid.org/0000-0002-8219-9505
Jon M. Jenkins https://orcid.org/0000-0002-4715-9460
George R. Ricker https://orcid.org/0000-0003-2058-6662
Sara Seager https://orcid.org/0000-0002-6892-6948
Roland K. Vanderspek https://orcid.org/0000-0001-6763-6562
Joshua N. Winn https://orcid.org/0000-0002-4265-047X

References

Adams, F. C., & Laughlin, G. 2003, Icar, 163, 290
Batygin, K. 2012, Natur, 491, 418
Batygin, K., Bodenheimer, P. H., & Laughlin, G. P. 2016, ApJ, 829, 114
Becker, J., Batygin, K., Fabrycky, D., et al. 2020, AJ, 160, 254
Becker, J. C., Vanderburg, A., Adams, F. C., Rappaport, S. A., & Schwengeler, H. M. 2015, ApJL, 812, L18
Bieryla, A., Zhou, G., García-Mejía, J., et al. 2024, MNRAS, 527, 10955
Boley, A. C., Granados Contreras, A. P., & Gladman, B. 2016, ApJL, 817, L17
Bonomo, A. S., Santerne, A., Alonso, R., et al. 2010, A&A, 520, A65
Bonomo, A. S., Sozzetti, A., Santerne, A., et al. 2015, A&A, 575, A85
Bouchy, F., Díaz, R. F., Hébrard, G., et al. 2013, A&A, 549, A49
Bouchy, F., Hébrard, G., Udry, S., et al. 2009, A&A, 505, 853
Brahm, R., Jordán, A., & Espinoza, N. 2017, PASP, 129, 034002
Brown, T. M., Baliber, N., Bianco, F. B., et al. 2013, PASP, 125, 1031
Buchhave, L. A., Bakos, G. Á., Hartman, J. D., et al. 2010, ApJ, 720, 1118
Buchhave, L. A., Latham, D. W., Johansen, A., et al. 2012, Natur, 486, 375
Cañas, C. I., Wang, S., Mahadevan, S., et al. 2019, ApJL, 870, L17
Caldwell, D. A., Tenenbaum, P., Twicken, J. D., et al. 2020, RNAAS, 4, 201
Chatterjee, S., Ford, E. B., Matsumura, S., & Rasio, F. A. 2008, ApJ, 686, 580
Chen, J., & Kipping, D. 2017, ApJ, 834, 17
Choi, J., Dotter, A., Conroy, C., et al. 2016, ApJ, 823, 102
Collier Cameron, A., Ford, E. B., Shahaf, S., et al. 2021, MNRAS, 505, 1699
Collins, K. 2019, AAS, 233, 140.05
Collins, K. A., Kielkopf, J. F., Stassun, K. G., & Hessman, F. V. 2017, AJ, 153, 77
Cosentino, R., Lovis, C., Pepe, F., et al. 2012, SPIE, 8446, 84461V
Cosentino, R., Lovis, C., Pepe, F., et al. 2014, SPIE, 9147, 91478C
Cutri, R. M., Skrutskie, M. F., van Dyk, S., et al. 2003, yCat,
Cutri, R. M., Wright, E. L., Conrow, T., et al. 2012, yCat,
Dai, F., Masuda, K., & Winn, J. N. 2018, ApJL, 864, L38
Dawson, R. I., Murray-Clay, R. A., & Johnson, J. A. 2015, ApJ, 798, 66
de Beurs, Z. L., Vanderburg, A., Shallue, C. J., et al. 2022, AJ, 164, 49
Donati, J.-F., Semel, M., Carter, B. D., Rees, D. E., & Collier Cameron, A. 1997, MNRAS, 291, 658
Dong, J., Huang, C. X., Zhou, G., et al. 2021, ApJL, 920, L16
Dong, J., Wang, S., Rice, M., et al. 2023, ApJL, 951, L29
Dotter, A. 2016, ApJS, 222, 8
Dumusque, X., Cretignier, M., Sosnowska, D., et al. 2021, A&A, 648, A103
Eastman, J., Gaudi, B. S., & Agol, E. 2013, PASP, 125, 83
Eastman, J. D., Rodriguez, J. E., Agol, E., et al. 2019, arXiv, arXiv:1907.09480
Fabrycky, D., & Tremaine, S. 2007, ApJ, 669, 1298
Fabrycky, D. C., Lissauer, J. J., Ragozzine, D., et al. 2014, ApJ, 790, 146

Fűrész, G. 2008, PhD thesis, University of Szeged, Hungary, https://doktori.bibl.u-szeged.hu/id/eprint/1135/
Fressin, F., Torres, G., Charbonneau, D., et al. 2013, ApJ, 766, 81
Fulton, B. J., Rosenthal, L. J., Hirsch, L. A., et al. 2021, ApJS, 255, 14
Gaia Collaboration, Brown, A. G. A., Vallenari, A., et al. 2018, A&A, 616, A1
Giacalone, S., Dressing, C. D., Jensen, E. L. N., et al. 2021, AJ, 161, 24
Goldreich, P., & Tremaine, S. 1980, ApJ, 241, 425
Gupta, A. F., Millholland, S. C., Im, H., et al. 2024, Natur, 632, 50
Halverson, S., Terrien, R., Mahadevan, S., et al. 2016, SPIE, 9908, 99086P
Hébrard, G., Bouchy, F., Pont, F., et al. 2008, A&A, 488, 763
Høg, E., Fabricius, C., Makarov, V. V., et al. 2000, A&A, 355, L27
Hord, B. J., Colón, K. D., Berger, T. A., et al. 2022, AJ, 164, 13
Huang, C., Wu, Y., & Triaud, A. H. M. J. 2016, ApJ, 825, 98
Huang, C. X., Quinn, S. N., Vanderburg, A., et al. 2020a, ApJL, 892, L7
Huang, C. X., Vanderburg, A., Pál, A., et al. 2020b, RNAAS, 4, 204
Huang, C. X., Vanderburg, A., Pál, A., et al. 2020c, RNAAS, 4, 206
Jenkins, J. M., Caldwell, D. A., Chandrasekaran, H., et al. 2010, ApJL, 713, L87
Jenkins, J. M., Twicken, J. D., Batalha, N. M., et al. 2015, AJ, 150, 56
Jenkins, J. M., Twicken, J. D., McCauliff, S., et al. 2016, SPIE, 9913, 99133E
Jensen, E. 2013, Tapir: A web interface for transit/eclipse observability, Astrophysics Source Code Library, ascl:1306.007
Kaufer, A., Stahl, O., Tubbesing, S., et al. 1999, Msngr, 95, 8
Knutson, H. A., Fulton, B. J., Montet, B. T., et al. 2014, ApJ, 785, 126
Korth, J., Chaturvedi, P., Parviainen, H., et al. 2024, ApJL, 971, L28
Kozai, Y. 1962, AJ, 67, 591
Kraus, A. L., Ireland, M. J., Huber, D., Mann, A. W., & Dupuy, T. J. 2016, AJ, 152, 8
Lester, K. V., Matson, R. A., Howell, S. B., et al. 2021, AJ, 162, 75
Lidov, M. L. 1962, P&SS, 9, 719
Lienhard, F., Mortier, A., Buchhave, L., et al. 2022, MNRAS, 513, 5328
Lin, D. N. C., Bodenheimer, P., & Richardson, D. C. 1996, Natur, 380, 606
Lindegren, L., Hernández, J., Bombrun, A., et al. 2018, A&A, 616, A2
Lissauer, J. J. 1993, ARA&A, 31, 129
Maciejewski, G., Golonka, J., Łoboda, W., et al. 2023, MNRAS, 525, L43
Madhusudhan, N., Amin, M. A., & Kennedy, G. M. 2014, ApJL, 794, L12
Matson, R. A., Howell, S. B., Horch, E. P., & Everett, M. E. 2018, AJ, 156, 31
McCully, C., Volgenau, N. H., Harbeck, D.-R., et al. 2018, SPIE, 10707, 107070K
Millholland, S. C., He, M. Y., Ford, E. B., et al. 2021, AJ, 162, 166
Mordasini, C., van Boekel, R., Mollière, P., Henning, T., & Benneke, B. 2016, ApJ, 832, 41
Moutou, C., Hébrard, G., Bouchy, F., et al. 2009, A&A, 498, L5
Mustill, A. J., Davies, M. B., & Johansen, A. 2015, ApJ, 808, 14
Naef, D., Latham, D. W., Mayor, M., et al. 2001, A&A, 375, L27
Naoz, S., Farr, W. M., Lithwick, Y., Rasio, F. A., & Teyssandier, J. 2011, Natur, 473, 187
Narita, N., Fukui, A., Kusakabe, N., et al. 2019, JATIS, 5, 015001
Narita, N., Fukui, A., Yamamuro, T., et al. 2020, SPIE, 11447, 114475K
NExScI 2022, Exoplanet Follow-up Observing Program Web Service, IPAC, doi:10.26134/EXOFOP5
Ngo, H., Knutson, H. A., Hinkley, S., et al. 2016, ApJ, 827, 8
Öberg, K. I., Murray-Clay, R., & Bergin, E. A. 2011, ApJL, 743, L16
Paredes, L. A., Henry, T. J., Quinn, S. N., et al. 2021, AJ, 162, 176
Parviainen, H., Tingley, B., Deeg, H. J., et al. 2019, A&A, 630, A89
Paxton, B., Bildsten, L., Dotter, A., et al. 2011, ApJS, 192, 3
Paxton, B., Cantiello, M., Arras, P., et al. 2013, ApJS, 208, 4
Paxton, B., Marchant, P., Schwab, J., et al. 2015, ApJS, 220, 15
Perruchot, S., Kohler, D., Bouchy, F., et al. 2008, SPIE, 7014, 70140J
Pollacco, D., Skillen, I., Collier Cameron, A., et al. 2008, MNRAS, 385, 1576
Quinn, S. 2025, TESS data from Quinn et al., "TOI-2494c and TOI-5143c: a hot Saturn and a hot Jupiter with interior planetary companions", STScI/MAST, doi:10.17909/ARZ7-BT05
Quinn, S. N., White, R. J., Latham, D. W., et al. 2014, ApJ, 787, 27
Raghavan, D., McAlister, H. A., Henry, T. J., et al. 2010, ApJS, 190, 1
Rice, M., Wang, S., Wang, X.-Y., et al. 2022, AJ, 164, 104
Ricker, G. R., Winn, J. N., Vanderspek, R., et al. 2015, JATIS, 1, 014003
Rodriguez, J. E., Quinn, S. N., Vanderburg, A., et al. 2023, MNRAS, 521, 2765
Rogers, T. M., Lin, D. N. C., & Lau, H. H. B. 2012, ApJL, 758, L6
Safonov, B. S., Lysenko, P. A., & Dodin, A. V. 2017, AstL, 43, 344
Schlaufman, K. C. 2010, ApJ, 719, 602
Schlecker, M., Kossakowski, D., Brahm, R., et al. 2020, AJ, 160, 275
Schulte, J., Rodriguez, J. E., Bieryla, A., et al. 2024, AJ, 168, 32
Schwab, C., Rakich, A., Gong, Q., et al. 2016, SPIE, 9908, 99087H
Scott, N. J., Howell, S. B., Horch, E. P., & Everett, M. E. 2018, PASP, 130, 054502
Sha, L., Vanderburg, A. M., Huang, C. X., et al. 2023, MNRAS, 524, 1113
Sha, L., Vanderburg, A. M., Huang, C. X., et al. 2026, arXiv:2601.13302
Shallue, C. J., & Vanderburg, A. 2018, AJ, 155, 94
Socrates, A., Katz, B., Dong, S., & Tremaine, S. 2012, ApJ, 750, 106
Spalding, C., & Batygin, K. 2017, AJ, 154, 93
Stassun, K. G., Oelkers, R. J., Paegert, M., et al. 2019, AJ, 158, 138
Stassun, K. G., Oelkers, R. J., Pepper, J., et al. 2018, AJ, 156, 102
Steffen, J. H., Ragozzine, D., Fabrycky, D. C., et al. 2012, PNAS, 109, 7982
Stumpe, M. C., Smith, J. C., Van Cleve, J. E., et al. 2012, PASP, 124, 985
Tinetti, G., Drossart, P., Eccleston, P., et al. 2018, ExA, 46, 135
Tokovinin, A. 2018, PASP, 130, 035002
Tokovinin, A., Fischer, D. A., Bonati, M., et al. 2013, PASP, 125, 1336
Tremaine, S., & Dong, S. 2012, AJ, 143, 94
Vanderburg, A., Huang, C. X., Rodriguez, J. E., et al. 2019, ApJL, 881, L19
Vanderburg, A., & Johnson, J. A. 2014, PASP, 126, 948
Wang, X.-Y., Rice, M., Wang, S., et al. 2024, ApJL, 973, L21
Williams, J., Krijt, S., Bitsch, B., Houge, A., & Bergner, J. 2025, MNRAS, 544, 3562
Winn, J. N., Fabrycky, D., Albrecht, S., & Johnson, J. A. 2010, ApJL, 718, L145
Wright, E. L., Eisenhardt, P. R. M., Mainzer, A. K., et al. 2010, AJ, 140, 1868
Wu, D.-H., Rice, M., & Wang, S. 2023, AJ, 165, 171
Wu, Y., & Lithwick, Y. 2011, ApJ, 735, 109
Xiang-Gruess, M. 2016, MNRAS, 455, 3086
Yee, S. W., Winn, J. N., Hartman, J. D., et al. 2023, ApJS, 265, 1
Zhou, G., Huang, C. X., Bakos, G. Á., et al. 2019, AJ, 158, 141
Zhou, G., Rodriguez, J. E., Vanderburg, A., et al. 2018, AJ, 156, 93
Zhu, W., Petrovich, C., Wu, Y., Dong, S., & Xie, J. 2018, ApJ, 860, 101